Influence of nonlinear electrodynamics on time-dependent accretion dynamics around Kalb-Ramond black hole

Rana Muhammad Zulqarnain[1†] Orhan Donmez[2‡] G. Mustafa[3,4§] Abdelmalek Bouzenada[4,5♮]
Ertan Güdekli[6♯] Shukhrat Mardonov[7,8¶]

[1]School of Business, Xian International University, Xian, 710077, Shaanxi, China
[2]College of Engineering and Technology, American University of the Middle East, Egaila 54200, Kuwait
[3]Department of Physics, Zhejiang Normal University, Jinhua 321004, People's Republic of China
[4]Research Center of Astrophysics and Cosmology, Khazar University, Baku, AZ1096, 41 Mehseti Street, Azerbaijan
[5]Laboratory of Theoretical and Applied Physics, Echahid Cheikh Larbi Tebessi University 12001, Algeria
[6]Department of Physics, Faculty of Science, Istanbul University, 34134, Istanbul, Turkey
[7]New Uzbekistan University, Movarounnahr str. 1, Tashkent 100000, Uzbekistan
[8]Ulugh Beg Astronomical Institute, Uzbekistan Academy of Sciences Tashkent, 100052, Uzbekistan

Abstract: In this paper, we analyze the dynamics of test particles in a Kalb-Ramond black hole (BH) spacetime coupled to nonlinear electrodynamics. After explicitly constructing the corresponding BH metric, including the nonlinear electromagnetic contributions to the geometry, we study the geodesic equations, focusing on the effective potential, the innermost stable circular orbits (ISCOs), and test-particle trajectories. This provides a quantitative description of orbital motion under the combined gravitational, Kalb-Ramond, and nonlinear electromagnetic effects. We then examine small perturbations of circular geodesics and derive the associated epicyclic frequencies for local and distant observers. These results show how the Kalb-Ramond field and nonlinear electrodynamics influence orbital stability, quasi-periodic oscillations (QPOs), and possible high-energy astrophysical signatures. Next, we numerically model Bondi-Hoyle-Lyttleton (BHL) accretion onto Kalb-Ramond BHs to assess how spacetime parameters affect flow morphology and dynamics. As the deformation parameters increase, the shock cone becomes more collimated, the stagnation point moves closer to the event horizon, and the matter density inside the cone decreases. For small deformations, QPO frequencies exhibit systematic shifts with enhanced oscillation amplitudes, whereas strong deformations damp the oscillations and produce a smooth, quasi-steady accretion rate. In this way, we illustrate a direct connection between spacetime geometry, shock-cone structure, and accretion variability, demonstrating that accretion dynamics serve as a sensitive probe of Kalb-Ramond BH spacetimes.

Keywords: Kalb-Ramond black holes, Nonlinear electrodynamics, Bondi-Hoyle-Lyttleton

DOI: 10.1088/1674-1137/ae66d0 **CSTR:**

I. INTRODUCTION

Kalb-Ramond gravity, originally formulated, explained, and defined by M. Kalb and P. Ramond through antisymmetric tensor gauge fields [1], constitutes a theoretically justified extension of Einstein's general relativity (GR) that arises naturally in higher-dimensional field theories and string-motivated constructions [2, 3]. The central element of this framework is the Kalb-Ramond field, defined as a rank-two antisymmetric tensor that augments the spacetime metric and generates additional propagating degrees of freedom not present in standard Riemannian gravity [4]. From a fundamental viewpoint, this tensor field belongs to the massless sector of closed string spectra, thereby showing a concrete and direct connection between gravitational dynamics and string-theoretic formulations [5]. In this context, Kalb-Ramond gravity provides a consistent theoretical setting to analyze deviations from Einstein gravity induced by extra tensorial fields that are well motivated by ultraviolet-complete theories [6]. Within this generalized framework, the interaction between the antisymmetric tensor field and the grav-

Received 5 March 2026; Accepted 23 April 2026
† E-mail: ranazulqarnain7777@gmail.com
‡ E-mail: orhan.donmez@aum.edu.kw
§ E-mail: gmustafa3828@gmail.com
♮ E-mail: abdelmalekbouzenada@gmail.com
♯ E-mail: gudekli@istanbul.edu.tr
¶ E-mail: shuhrat˙mardonov@yahoo.com

itational sector produces nontrivial corrections to the spacetime geometry and to the corresponding field equations, especially in regimes where higher-dimensional or string-scale effects are relevant [7]. These corrections have motivated extensive studies of Lorentz symmetry violation and spontaneous symmetry breaking in gravitational models, where antisymmetric background fields naturally arise and play an essential dynamical role [8]. Related analyses have clarified the phenomenological consequences of tensor fields coupled to gravity, particularly within effective field theory descriptions designed to encode low-energy manifestations of Planck-scale physics [9]. In this setting, Kalb-Ramond-type fields have also been investigated in relation to modified electromagnetic sectors and gravitational birefringence, strengthening the physical motivation for their inclusion in extended theories of gravity [10−22].

The influence of Kalb-Ramond gravity is particularly manifest in black hole (BH) frameworks, where antisymmetric tensor fields introduce additional geometric degrees of freedom capable of modifying both local and global properties of BH solutions [23]. The presence of the antisymmetric sector leads to quantitative corrections in the horizon structure, induces shifts in thermodynamic quantities, and illustrates particle dynamics in the vicinity of the BH through modified effective potentials and conserved quantities [24]. Many analyses have established that Kalb-Ramond fields influence geodesic motion, gravitational lensing, and stability criteria of compact objects, thereby generating potentially measurable signatures in astrophysical and cosmological regimes [25, 26]. Furthermore, the simultaneous inclusion of Kalb-Ramond fields and nonlinear electrodynamics enables the construction of regular or string-inspired BH solutions whose metric functions deviate from the standard Reissner-Nordström geometry at short and intermediate scales [27]. Beyond BH configurations, antisymmetric tensor fields have been systematically tested in cosmological and semiclassical gravity contexts, where they can affect early-universe dynamics, dark sector parametrizations, and effective vacuum polarization processes through additional coupling terms [28]. Their impact has also been assessed within gravitational lensing and optical geometry analyses, which provide precise diagnostics of strong-field departures from GR via null geodesic structure and deflection observables [29, 30]. Concurrent studies of Hawking radiation, quantum tunneling processes, and horizon thermodynamics in extended gravitational theories indicate that Kalb-Ramond and related fields produce nontrivial modifications to BH evaporation rates and entropy relations [31, 32]. These results are directly connected to fundamental studies of gauge fields, classical gravity, and horizon thermodynamics, which constitute the theoretical basis of semiclassical and quantum gravity formalisms [33, 34]. From a formal perspective, Kalb-Ramond gravity illustrates a GR-like construction embedded in an enlarged geometric and field-theoretic framework, contributing to unification programs that incorporate gravity within a broader gauge structure [35]. Its compatibility with classical solutions, including electrovacuum and scalar-tensor models, further supports its consistency as an effective extension of GR at the classical level [36, 37]. Given the strong experimental confirmation of GR [38, 39], Kalb-Ramond gravity can therefore be regarded as a theoretically controlled generalization that introduces additional propagating modes without contradicting established tests. On the other hand, Kalb-Ramond black holes in ModMax electrodynamics exhibit significantly modified particle orbits, thermodynamic stability, and observable signatures, with pronounced differences between the ordinary and phantom branches [40]. Consequently, this framework provides a systematic setting to probe spacetime structure, gravitational dynamics in the presence of extra fields, and the interface between classical gravity and quantum theory [41−44].

QPOs constitute a primary observable in X-ray timing analyses aimed at identifying the dynamical processes governing accretion onto compact objects, and they have been conclusively detected in numerous neutron star and BH binary systems through high-time-resolution measurements [45−56]. In the Fourier domain, QPOs appear as narrow, statistically significant peaks superposed on a broadband noise component in the power density spectrum, illustrating the action of coherent or semi-coherent oscillatory modes embedded within an intrinsically stochastic accretion flow [57−60]. The measured QPO frequencies extend from millihertz to kilohertz regimes, reflecting a spectrum of characteristic dynamical timescales associated with disk structure, orbital motion, and relativistic effects operating in the strong-field region around compact objects [61−63]. In this framework, low-frequency QPOs are generally attributed to global disk phenomena, including Lense-Thirring precession driven by frame dragging, disk warping, and large-scale magnetohydrodynamic instabilities, which are preferentially triggered when the angular momentum of the accretion flow is misaligned with the spin axis of the central object [64]. This broader accretion context is consistent with the hot-accretion and horizon-based phenomenology emphasized by [65], although our study focuses on dynamical shock-cone formation and variability in a deformed spacetime rather than on radiative ADAF spectra. High-frequency QPOs (HFQPOs), typically observed in the 10^2-10^3 Hz range, are commonly interpreted in terms of fundamental relativistic frequencies that govern particle motion in the innermost disk region, namely the Keplerian orbital frequency together with the radial and vertical epicyclic frequencies generated by spacetime curvature [66−80].

Moreover, HFQPOs are regarded as direct probes of

strong-gravity effects predicted by GR. In particular, X-ray timing observations of several Galactic microquasars, such as *GROJ*1655-40 [81], *XTEJ*1550-564 [82], *GRS*1915+105 [83], and *H*1743-322, have revealed pairs of HFQPOs exhibiting a stable 3:2 frequency ratio [84−86]. This persistent commensurability provides strong support for resonance-based scenarios, especially models involving non-linear coupling between radial and vertical epicyclic oscillation modes of accreting matter [87]. Within relativistic disk models, such resonances arise naturally because GR induces distinct radial and vertical epicyclic frequencies, allowing resonance conditions that are absent in Newtonian gravity [88−91]. An important consequence of this interpretation is the inverse dependence of QPO frequency on BH mass $\nu \propto 1/M$, which provides an observational tool to constrain intrinsic BH parameters, particularly the mass and dimensionless spin [92]. Applying this scaling to the HFQPO data frequently implies rapidly rotating BH configurations, with typical spin parameters in the interval $a \approx 0.8$-0.96 [93]. Although alternative mechanisms, including diskoseismic modes, orbiting hot-spot models, and higher-order harmonic effects, have been proposed [94−97], resonance-based frameworks remain the most consistent with both the observed frequency ratios and their temporal stability. Furthermore, while analogous oscillatory features are observed in neutron star and white dwarf accretion systems, persistent twin-peak HFQPOs with fixed ratios appear to be characteristic of BH binaries, reinforcing the conclusion that these signals originate from strong-field gravitational dynamics in the vicinity of the event horizon [98−100].

The organization of this work is structured as follows: Section (II) presents the explicit construction of the Kalb-Ramond BH metric models with nonlinear electrodynamics, specifying the spacetime geometry, the functional form of the metric coefficients, and the complete set of Einstein and field equations governing the coupled gravitational and nonlinear electrodynamic sectors. Section (III) examines geodesic motion in these spacetimes, providing a detailed investigation of the effective potential governing particle motion (III A), the exact determination of ISCOs through stability conditions (III B), and a quantitative description of particle trajectories in the vicinity of the BHs (III C). Section (IV) analyzes harmonic oscillations as perturbations of circular orbits, deriving the associated characteristic frequencies and establishing their dependence on BH and field parameters, as measured by local observers (IV A) and distant observers (IV B). In this context, this structured formulation ensures a comprehensive assessment of particle dynamics, stability criteria, and potential observational signatures in Kalb-Ramond BHs modified by nonlinear electrodynamic effects. In Section (V), by numerically solving the fully general relativistic hydrodynamics (GRH) equations in a fixed Kalb-Ramond spacetime, we investigate the effects of spacetime deformation parameters on the dynamical evolution of the shock cone formed through the BHL accretion mechanism around Kalb-Ramond BHs coupled to nonlinear electrodynamics, and discuss the testability and observability of Kalb-Ramond BHs.

II. KALB-RAMOND BH METRIC MODELS WITH NONLINEAR ELECTRODYNAMICS

In this section, the spacetime of a static, spherically symmetric Kalb-Ramond BH model coupled to nonlinear electrodynamics is described by the line element given in [101]:

$$ds^2 = -h(r)dt^2 + h^{-1}(r)dr^2 + d\mathcal{H}^2_{2\mathcal{D}}, \tag{1}$$

where $d\mathcal{H}^2_{2\mathcal{D}} = r^2(d\theta^2 + \sin^2\theta\, d\phi^2)$, and the metric function $h(r)$ is explicitly given by:

$$h(r) = \left(\frac{1}{1-\alpha}\right)\left[1 + \frac{\beta Q^2}{(1-\alpha)r^2}\right] e^{-\eta} - \frac{2M}{r}. \tag{2}$$

Here, M denotes the BH mass, whereas α encodes the Lorentz symmetry-breaking contribution generated by the Kalb-Ramond background field. Additionally, the event horizon associated with the metric (1) follows directly from the root structure defined by the condition $h(r) = 0$. In this case, Fig. 1 illustrates the functional behavior of the metric function $h(r)$ for different values of the parameter α. One also finds that a larger α systematically increases the amplitude of $h(r)$ throughout the entire exterior spacetime region.

To elucidate the physical structure of the obtained configuration, it is necessary to examine the parametric limits of the BH model solution and establish its correspondence with the Schwarzschild geometry. In this case, the limit $\beta \to 0$ suppresses the nonlinear electrodynamics sector, thereby eliminating the electromagnetic correction to the metric function. Also, the condition $Q \to 0$ removes the charge contribution completely and, in particular, cancels the r^{-2} term originating from the electromagnetic field. Imposing $\eta \to 0$ suppresses the exponential deformation factor, restoring the standard radial dependence. Furthermore, the limit $\alpha \to 0$ deactivates the Lorentz symmetry-breaking effect associated with the Kalb-Ramond background field. When the combined limits $\alpha \to 0$, $\beta \to 0$, $Q \to 0$, and $\eta \to 0$ are applied simultaneously, the metric function reduces to $h(r) = 1 - \frac{2M}{r}$, which is identical to the Schwarzschild solution. In this limit, the spacetime becomes asymptotically flat in the standard sense, the event horizon is located at $r_h = 2M$, and all corrections induced by nonlinear electrodynamics

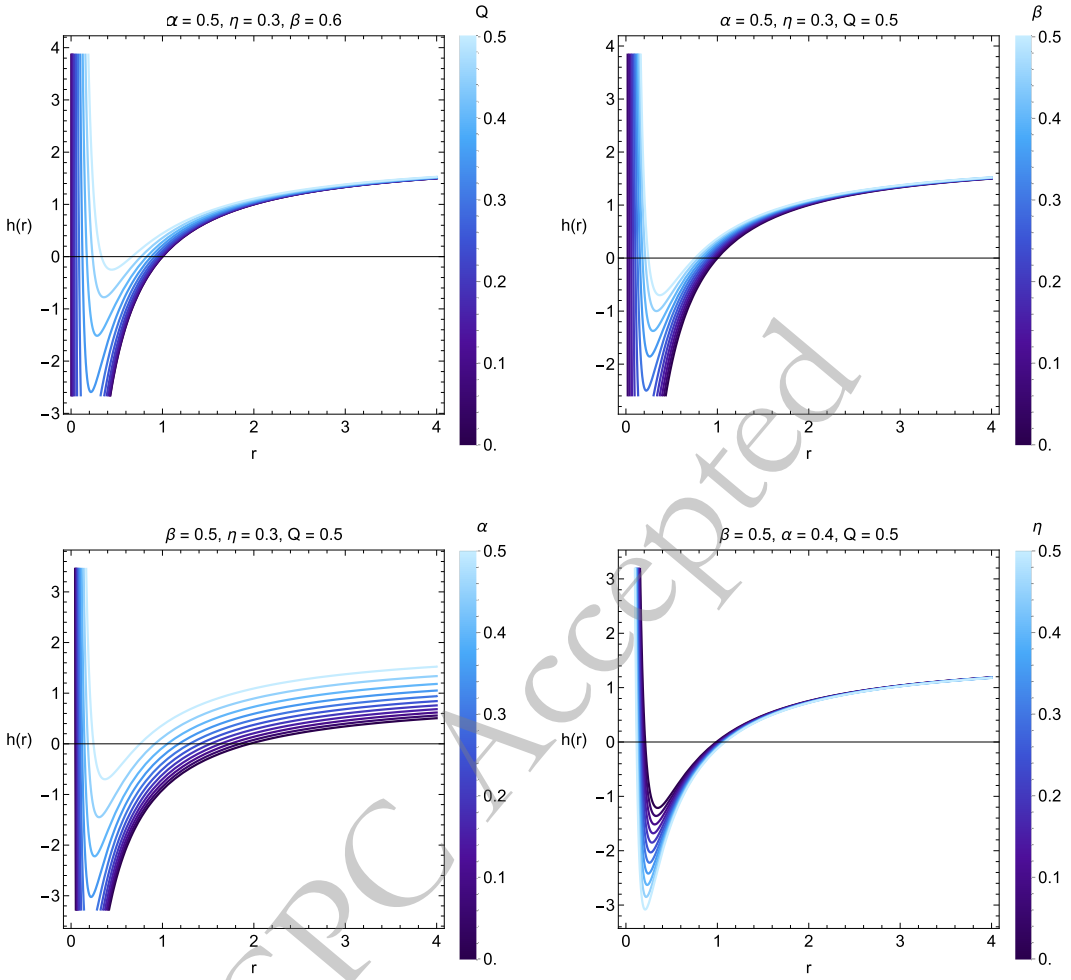

Fig. 1. (color online) Behavior of the metric function of the Kalb-Ramond BHs with nonlinear electrodynamics.

and Lorentz-violating background fields vanish. Thus, the present model constitutes a consistent extension of the Schwarzschild geometry, where deviations from the classical solution are fully governed by the parameters (α,β,Q,η), and the Schwarzschild BH is recovered continuously in the appropriate parametric regime.

The location of the event horizon is obtained from the condition $(h(r)=0)$; however, a complete geometrical analysis requires verifying the absence of nonphysical singularities beyond the central singularity at $(r=0)$. In particular, the structure of the metric function involves the prefactor $((1-\alpha)^{-1})$ and the exponential contribution $(e^{-\eta})$, which may introduce pathological behavior for specific parameter ranges. Also, the factor $((1-\alpha)^{-1})$ acts multiplicatively on the metric components and directly affects their regularity properties. In this case, the limit $(\alpha \to 1)$ leads to a divergence in the metric coefficients, signaling a breakdown of the spacetime description rather than a physical singularity. Although the exponential term remains finite for regular values of (η), its contribution modifies the radial dependence of the geometry and can influence the asymptotic structure. Consequently, any implicit dependence of (η) on the radial coordinate or other parameters must be examined to exclude hidden divergences or ill-defined regions. In this context, a consistent parameter domain $((\alpha,\beta,Q,\eta))$ must be imposed to ensure that the metric function remains regular for $(r>0)$, guaranteeing that the only physical singularity is located at the origin, while all other features correspond to coordinate or removable singularities.

The exponential deformation factor $(e^{-\eta})$ appearing in the metric function is not introduced phenomenologically; rather, it represents effective modifications generated by the nonlinear electrodynamics (NLED) sector coupled consistently to the Kalb-Ramond background. Within a consistent theoretical construction, η must be defined as a dimensionless parameter built from electromagnetic invariants entering the NLED Lagrangian density, typically involving contractions of the field strength tensor that alter the standard Maxwell contribution in strong-field regimes. Moreover, its sign and magnitude are not arbitrary but are restricted by fundamental physical conditions such as spacetime regularity, positivity of the energy density, and dynamical stability of the electro-

magnetic sector. In this case, negative values ($\eta < 0$) produce an exponential enhancement of the metric function, which can induce unphysical behavior, including divergences in the asymptotic region or violations of standard energy conditions, and are thus excluded by consistency requirements. A complete determination of the allowed domain of η requires deriving the solution from an underlying action principle, where the explicit functional dependence of η follows directly from the selected NLED Lagrangian. In the absence of such a derivation, the parameter η should be treated as an effective phenomenological quantity, and the explored parameter space must be limited to regions ensuring the physical consistency of the spacetime geometry.

III. GEODESIC MOTION IN KALB-RAMOND BH GEOMETRY WITH NONLINEAR ELECTRODYNAMICS

In this section, we analyze the motion of a neutral test particle in a static Kalb-Ramond black hole (BH) model coupled to nonlinear electrodynamics. The particle's trajectory is described within the Hamiltonian formalism as [102−104]:

$$H = \frac{1}{2} g^{\mu\nu} p_\mu p_\nu + \frac{1}{2}\mu^2, \tag{3}$$

where μ denotes the particle's rest mass. The four-momentum is defined as $p^\alpha = \mu u^\alpha$, where $u^\alpha = dx^\alpha/d\tau$ is the four-velocity and τ is the proper time along the worldline. By following the procedure in [102−104], one obtains the following effective expression:

$$V_{eff}(r) = \left(1 + \frac{\mathcal{L}^2}{r^2}\right)\left(\frac{1}{1-\alpha} + \frac{\beta\left(Q^2\exp(-\eta)\right)}{(1-\alpha)^2 r^2} - \frac{2M}{r}\right). \tag{4}$$

By restricting the motion to the equatorial plane, $\theta = \pi/2$, consistent with the symmetry of the metric, the effective potential reduces to the following form:

$$V_{eff}(r) = \frac{e^{-\eta}\left(L^2 + r^2\right)\left(\beta Q^2 - (\alpha-1)e^{\eta} r(2\alpha + r - 2)\right)}{(\alpha-1)^2 r^4}. \tag{5}$$

The effective potential in Eq. (5) highlights the influence of the parameters α, β, Q, and M on the radial motion of a test particle. In particular, the factor $(\alpha-1)^2 r^4$ implies a divergence of the potential as $\alpha \to 1$, reflecting a limitation of the current parametrization in this regime. This divergence indicates that values of α approaching unity are physically inadmissible, since they produce singular behavior in the effective potential that is incompatible with a regular spacetime geometry.

The Schwarzschild limit is obtained in the formal case where the deformations vanish—specifically, $\alpha \to 0$, $\beta \to 0$, and $Q = 0$—reducing Eq. ((5)) to the standard Schwarzschild effective potential

$$V_{\text{eff}}^{\text{Schw}}(r) = \left(1 + \frac{L^2}{r^2}\right)\left(1 - \frac{2M}{r}\right). \tag{6}$$

This limit serves as an explicit consistency check, confirming that the model correctly reproduces the well-known general-relativistic behavior in the absence of deformations.

The parameter α is further restricted by the requirement that the spacetime remain free of singularities and dynamical instabilities. Specifically, $\alpha \geq 1$ leads to divergences in the effective potential and may correspond to naked singularities, thereby violating the cosmic censorship conjecture. Similarly, the parameters β and Q must be bounded to prevent pathologies arising from nonlinear electromagnetic contributions to the potential, ensuring that the effective potential remains finite and the spacetime is regular. Equation (5) explicitly illustrates the modification of test particle dynamics by each deformation parameter, while the reduction to the Schwarzschild case confirms the internal consistency of the framework. The physical range of α is thus constrained to $\alpha < 1$ to maintain a well-defined effective potential and a stable, regular spacetime structure.

A. Effective potential around Kalb-Ramond BHs with nonlinear electrodynamics

The effective potential $V_{\text{eff}}(r)$ is a fundamental diagnostic for quantifying the influence of black hole (BH) parameters on particle dynamics. The conditions derived below determine circular orbits in electrodynamics in the equatorial plane and provide a systematic method to locate and assess the stability of such orbits without explicitly integrating the full set of geodesic equations. In this framework, local minima of V_{eff} correspond to stable circular orbits, for which small radial perturbations produce bounded oscillations, whereas local maxima correspond to unstable circular orbits that are highly sensitive to radial perturbations, leading to escape or infall. Figure 2 displays the radial dependence of V_{eff} for representative values of the BH charge Q and the particle's angular momentum $\mathcal{L}$. A decrease in either Q or $\mathcal{L}$ reduces the depth of the potential well, indicating weaker effective binding and implying that the corresponding equilibrium circular orbits lie at larger radii. The necessary conditions for equatorial circular motion are given by [102−104]:

$$V_{\text{eff}}(r) = \mathcal{E}^2, \quad \frac{\mathrm{d}V_{\text{eff}}(r)}{\mathrm{d}r} = 0. \tag{7}$$

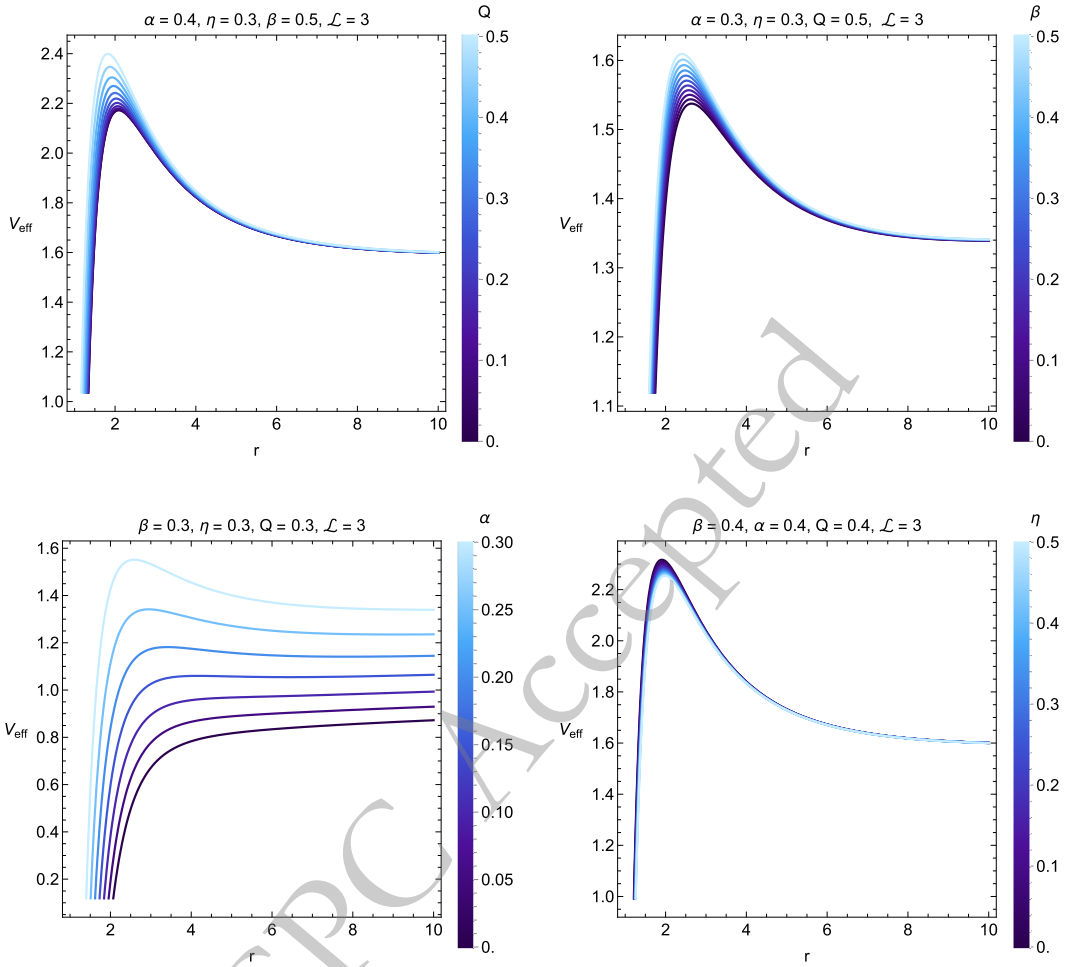

Fig. 2. (color online) The effective potential $V_{\rm eff}(r)$ for test particles in the background of a Kalb-Ramond BH with nonlinear electrodynamics.

From the relations above, one can determine the specific energy $\mathcal{E}$ and the specific angular momentum $\mathcal{L}$. In particular, solving Eq. (7) for a nonrotating KR black hole within the framework of nonlinear electrodynamics yields the following expression for the angular momentum:

$$\mathcal{L}=\frac{r\sqrt{r-\dfrac{\beta e^{-\eta}Q^2}{(\alpha-1)^2}}}{\sqrt{\dfrac{2\beta e^{-\eta}Q^2-(\alpha-1)r(3\alpha+r-3)}{(\alpha-1)^2}}}, \tag{8}$$

The associated energy is defined as:

$$\mathcal{E}=\frac{e^{-\eta}\left(\beta Q^2-(\alpha-1)e^{\eta}r(2\alpha+r-2)\right)}{(\alpha-1)^2 r\sqrt{\dfrac{2\beta e^{-\eta}Q^2-(\alpha-1)r(3\alpha+r-3)}{(\alpha-1)^2}}}. \tag{9}$$

In this context, these expressions explicitly incorporate the nonlinear contributions of the electromagnetic sector through the charge parameter Q and the exponential factor $e^{-\eta}$, thereby elucidating how departures from linear Maxwell electrodynamics affect the system's orbital characteristics.

Fig. 3 illustrates the dependence of the specific angular momentum $\mathcal{L}$ on the radial coordinate for test particles in equatorial circular orbits around a KR BH. Larger values of $\mathcal{L}$ correspond to deeper effective potential wells, enabling particles to sustain more tightly bound orbits at smaller radii. Fig. 4 presents the radial profile of the specific energy $\mathcal{E}$ of the orbiting particles. The energy increases monotonically with radial distance from the BH, reflecting the progressive weakening of the gravitational field at larger radii. Moreover, the profile exhibits a pronounced dependence on the BH charge Q, thereby highlighting the impact of nonlinear electrodynamic effects on the orbital energetics.

B. ISCOs

In this section, the ISCO is the minimum radius at which a test particle can maintain a stable circular orbit

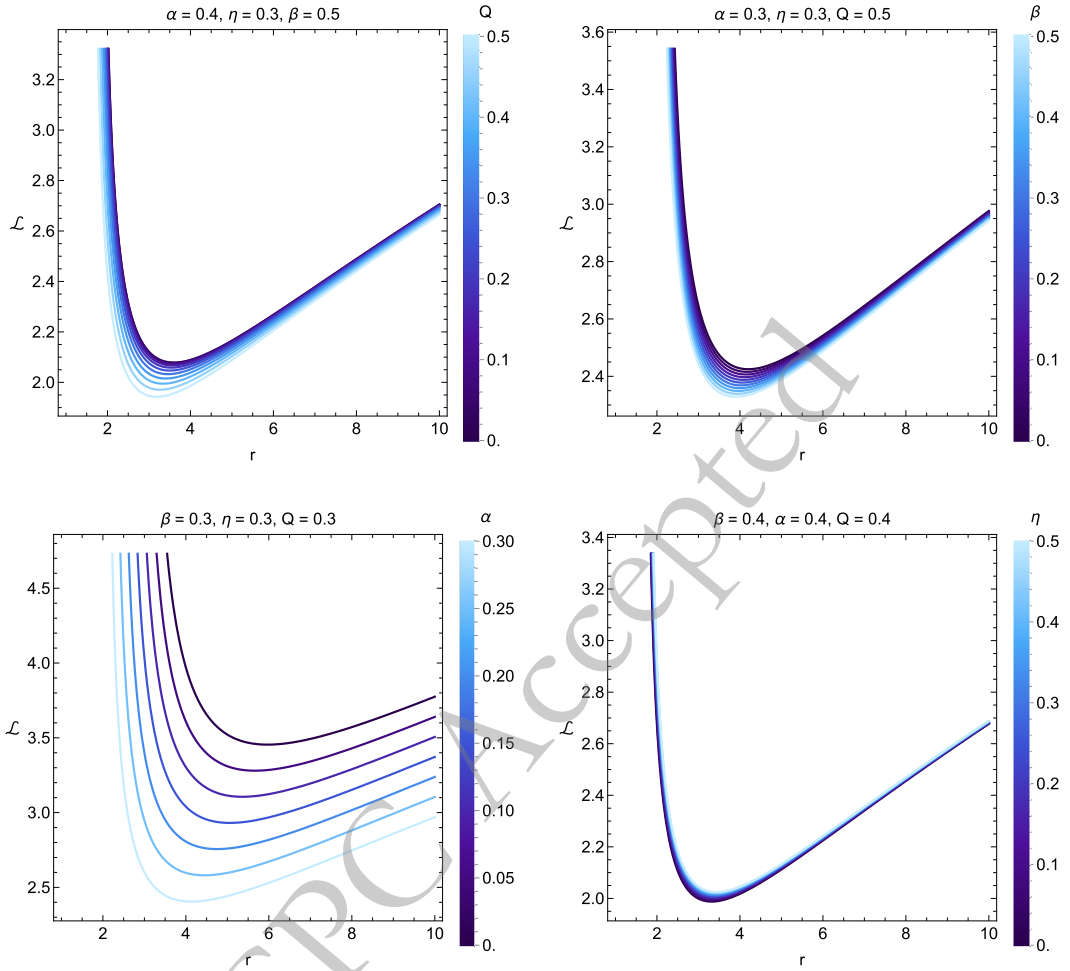

Fig. 3. (color online) Angular momentum of particles in equatorial circular orbits around a Kalb-Ramond black hole with nonlinear electrodynamics.

around a BH. It is determined by analyzing the effective potential, where local minima correspond to stable orbits and local maxima to unstable configurations. In Newtonian gravity, the effective potential exhibits a minimum for any finite angular momentum, implying that all circular orbits are stable and no innermost stable orbit exists. In GR, the effective potential depends explicitly on both the particle's angular momentum and the BH parameters, leading to a critical radius below which circular motion becomes dynamically unstable. For a Schwarzschild BH, this critical radius is $r = 3r_g$, where r_g denotes the gravitational radius. In the case of Kalb-Ramond BHs coupled to nonlinear electrodynamics, the ISCO parameters are obtained by solving the standard conditions [102−104] for the ISCO:

$$\frac{d^2V_{\rm eff}(r)}{dr^2} = 0. \tag{10}$$

The ISCO radii can be determined by solving the following equation:

$$\frac{e^{-\eta}\left(4\beta^2Q^4 - 9(\alpha-1)^2\beta e^{\eta}Q^2 r + (\alpha-1)^3 e^{2\eta}r^2(6\alpha+r-6)\right)}{2(\alpha-1)^2\left((\alpha-1)e^{\eta}r(3\alpha+r-3) - 2\beta Q^2\right)\sqrt{\frac{2\beta e^{-\eta}Q^2 - (\alpha-1)r(3\alpha+r-3)}{(\alpha-1)^2}}\sqrt{r - \frac{\beta e^{-\eta}Q^2}{(\alpha-1)^2}}} = 0.$$

An exact analytical expression for the ISCO radius is not feasible because the above equation is highly complicated. Nevertheless, we can compute and analyze the influence of the relevant parameters on the ISCO using nu-

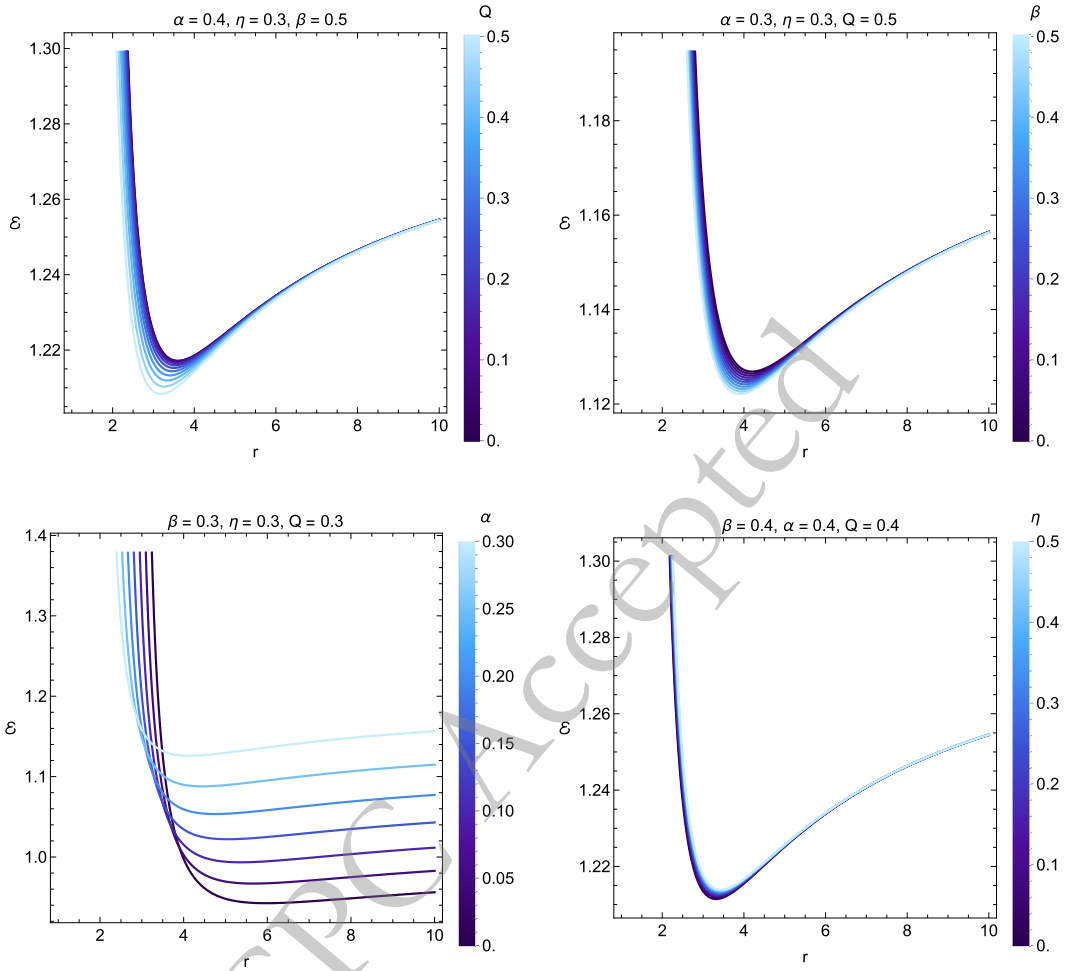

Fig. 4. (color online) Energy of particles in equatorial circular orbits around a Kalb–Ramond black hole with nonlinear electrodynamics.

merical methods. In this framework, the effective potential depends on the BH charge (Q) and the nonlinear electrodynamics parameters, leading to shifts in the ISCO radius relative to the Schwarzschild BH limit. Figure 5 quantifies how the ISCO radius varies with increasing BH charge, illustrating an outward displacement of stable orbits due to the combined gravitational and nonlinear electromagnetic effects.

C. Particle Trajectories around Kalb-Ramond BH models with nonlinear electrodynamics

In this section, we numerically integrate the equations of motion [102−104] for test particles in the background of a charged Kalb-Ramond BH with nonlinear electrodynamics. The resulting trajectories for different BH charge values are illustrated in Figs. (6) and (7). In each figure, the first row corresponds to the uncharged Schwarzschild BH limit ($Q=0$), while the subsequent rows depict configurations with $Q=0.5$ and $Q=0.7$, with all other parameters held fixed. Our computations reveal that increasing the BH charge (Q) extends the radial range of stable orbits and modifies the orbital geometry, reflecting the enhanced electromagnetic repulsion that counteracts gravitational attraction. These results highlight the influence of nonlinear electrodynamics on the orbital structure and elucidate the interplay between gravitational and electromagnetic effects in determining particle dynamics around Kalb-Ramond BHs.

IV. HARMONIC OSCILLATIONS MEASUREMENT AS PERTURBATIONS OF CIRCULAR ORBITS IN KALB-RAMOND BHS WITH NONLINEAR ELECTRODYNAMICS

In this section, we analyze the dynamics of small perturbations about stable circular orbits in the equatorial plane by considering neutral test particles subjected to minor displacements from their equilibrium positions. Such perturbations induce epicyclic motion that can be modeled as simple harmonic oscillations governed by the effective potential associated with the background space-

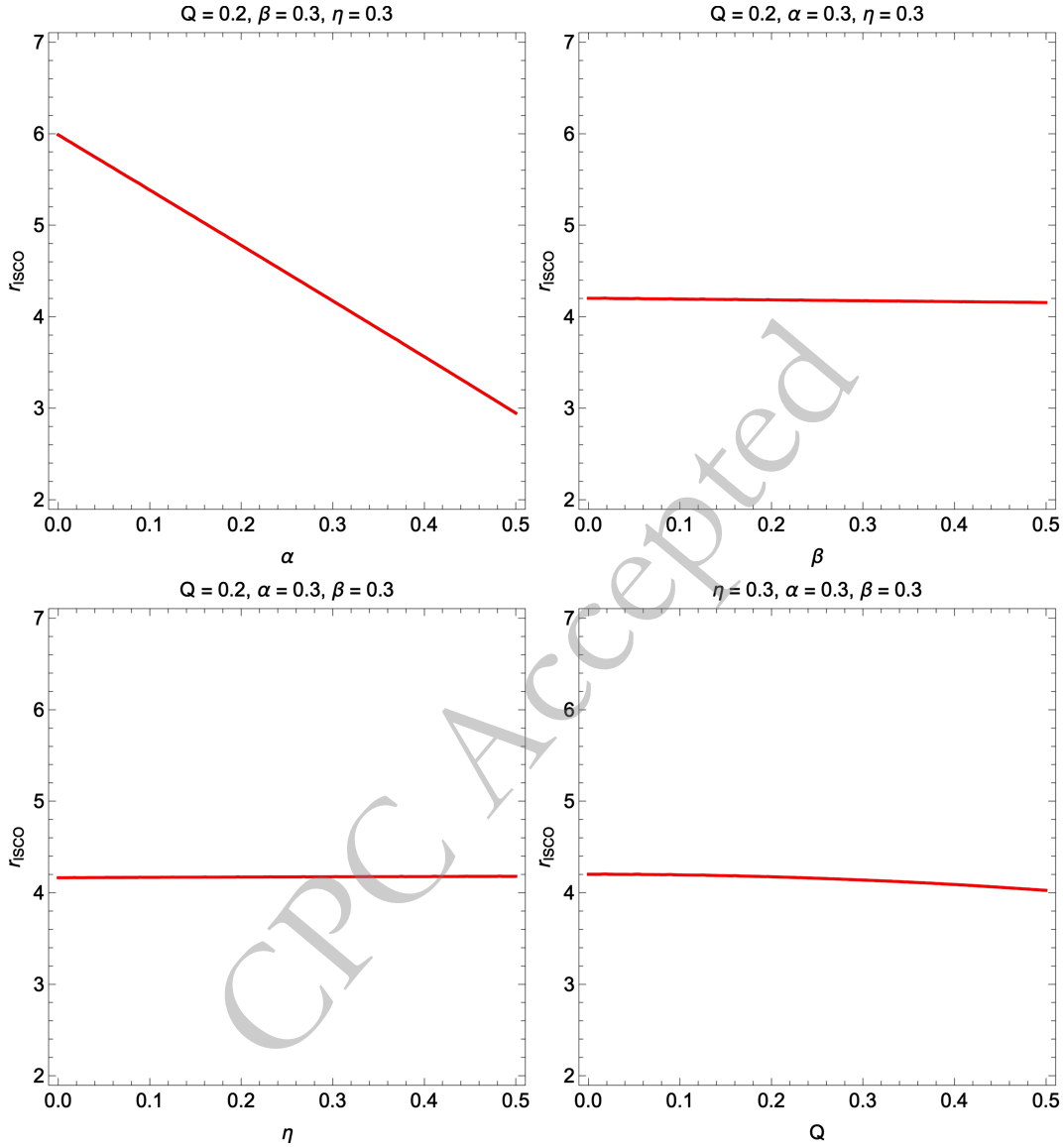

Fig. 5. (color online) ISCO radii of test particles orbiting a Kalb-Ramond BH in nonlinear electrodynamics.

time [102−104]. This framework provides a systematic approach for computing the radial, vertical, and azimuthal frequencies in the vicinity of a black hole (BH) described by a Kalb-Ramond metric coupled to nonlinear electrodynamics, explicitly accounting for modifications introduced by the gauge fields.

A. Frequencies Measured in the case of the Local Observer in Kalb-Ramond BHs with Nonlinear Electrodynamics

In this section, the exact epicyclic frequencies, as measured by a local observer comoving with the particle, are determined from the second derivatives of the effective potential $V_{\rm eff}(r,\theta)$ [102−104]:

$$\begin{aligned}\omega_r^2 &= -\frac{1}{2}\frac{\partial^2 V_{\rm eff}(r,\theta)}{\partial r^2},\\ \omega_\theta^2 &= \frac{1}{2}\frac{g_{rr}(r,\theta)}{r^2}\frac{\partial^2 V_{\rm eff}(r,\theta)}{\partial \theta^2},\\ \omega_\phi &= \frac{{\rm d}\phi}{{\rm d}\tau}.\end{aligned} \tag{11}$$

where ω_r, ω_θ, and ω_ϕ denote the radial, vertical, and azimuthal angular frequencies, respectively. In this case, these quantities depend explicitly on the BH model parameters, including contributions from the Kalb-Ramond field and the nonlinear electromagnetic charge, and they encode the response of particle trajectories to spacetime curvature and gauge interactions.

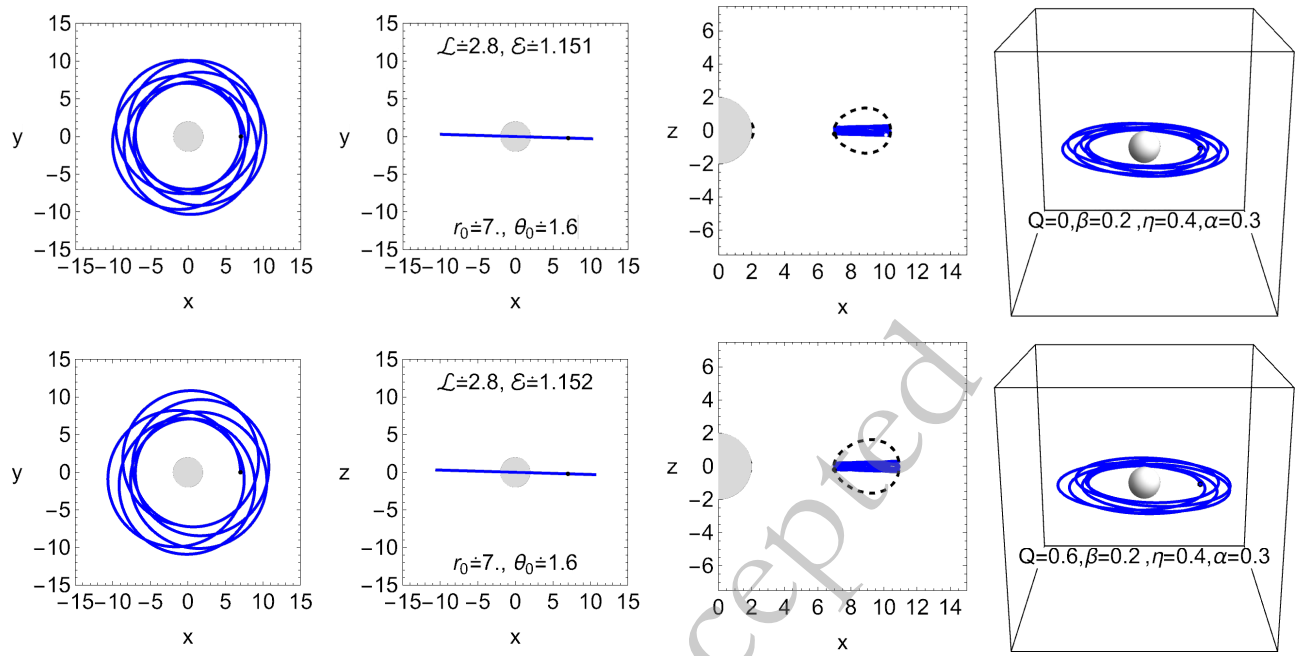

Fig. 6. (color online) Trajectories of test particles around a charged Kalb-Ramond black hole (BH) with nonlinear electrodynamics for various values of Q. The first row corresponds to the Schwarzschild BH case ($Q=0$).

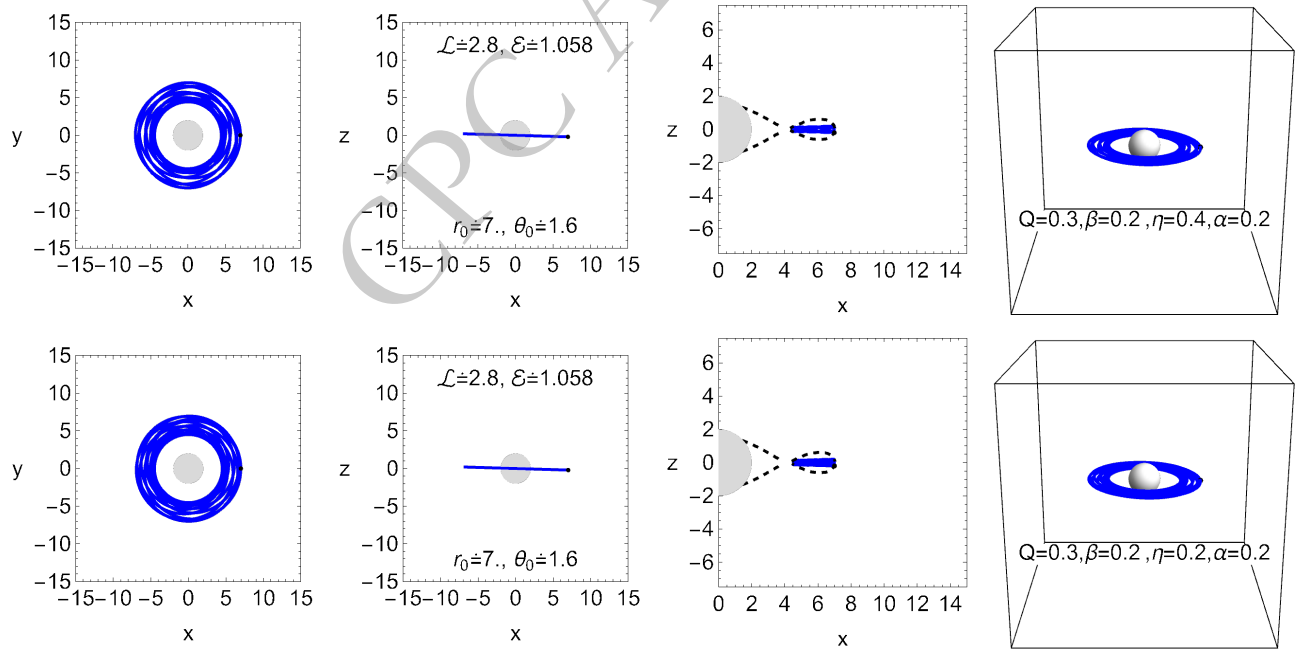

Fig. 7. (color online) Extended particle trajectories for varying black hole (BH) charge Q in the Kalb-Ramond metric with nonlinear electrodynamics. All other parameters are held fixed.

$$\omega_r = \frac{e^{-\eta}\left((\alpha-1)e^{\eta}r\left(3L^2(4\alpha+r-4)+2(\alpha-1)r^2\right)-\beta Q^2\left(10L^2+3r^2\right)\right)}{(\alpha-1)^2 r^6},$$
$$\omega_\theta = \frac{\beta Q^2-(\alpha-1)^2 e^{\eta}r}{r^2\left((\alpha-1)e^{\eta}r(3\alpha+r-3)-2\beta Q^2\right)}, \tag{12}$$

$$\omega_\phi = \frac{\beta Q^2-(\alpha-1)^2 e^{\eta}r}{r^2\left((\alpha-1)e^{\eta}r(3\alpha+r-3)-2\beta Q^2\right)}. \tag{13}$$

In the limit where nonlinear electromagnetic effects vanish, the epicyclic frequencies reduce to the standard Schwarzschild values for neutral particles, providing a consistency check and showing the influence of the additional fields on orbital dynamics.

Equations (12) yield identical values for the vertical and azimuthal epicyclic frequencies, ω_θ and ω_ϕ, thereby reflecting the leading-order spherical symmetry of the

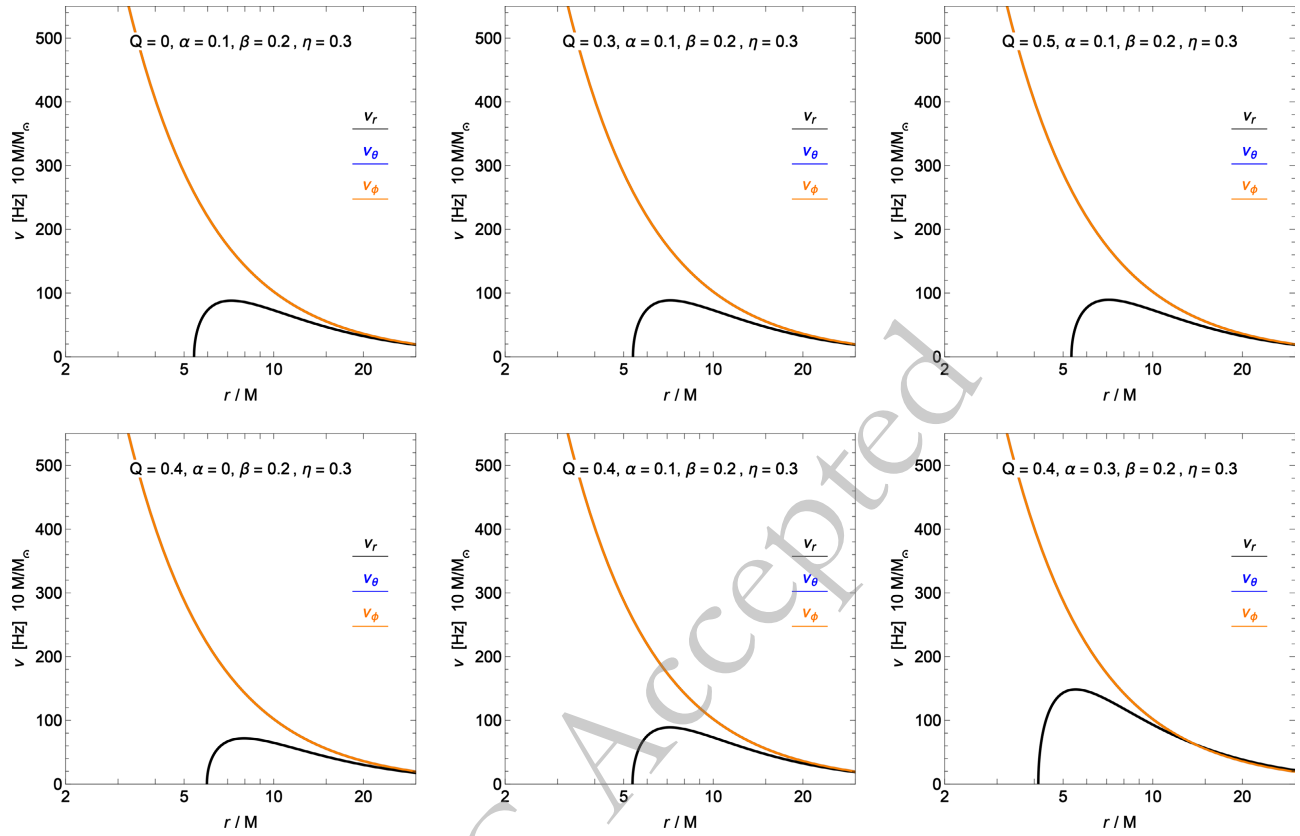

Fig. 8. (color online) Radial profiles of epicyclic frequencies for neutral test particles orbiting a non-rotating Kalb-Ramond black hole coupled to nonlinear electrodynamics, as measured by a local observer.

black hole (BH) spacetime. This equivalence arises because, at lowest order, the particle dynamics are dominated by the radial structure of the effective potential, while angular perturbations around circular orbits respond isotropically. In the context of a charged BH with nonlinear electrodynamics, however, the inclusion of the electromagnetic charge Q and the nonlinear coupling parameter β introduces additional contributions that couple the electromagnetic field to the spacetime curvature. These couplings modify the effective potential differently along the θ and ϕ directions, particularly when higher-order corrections in βQ^2 are included. As a result, the degeneracy $\omega_\theta = \omega_\phi$ can be lifted at second or higher perturbative orders, depending on the values of the BH mass, charge, the nonlinear parameter β, and any additional contributions from fields such as the Kalb-Ramond term α or metric modifications encoded in η. These corrections are expected to produce measurable deviations in the epicyclic frequencies, influencing orbital stability, precession rates, and resonant interactions near the BH. It is therefore essential to examine whether $\omega_\theta = \omega_\phi$ remains valid under second-order βQ^2 corrections in order to quantify the influence of nonlinear electrodynamics on test-particle motion in such spacetimes.

B. Frequencies Measured in the case of the Distant Observer in Kalb-Ramond BHs with Nonlinear Electrodynamics

For a static observer at asymptotic infinity, the measurable angular velocities Ω_β are obtained from the gravitational redshift relation [102−104]:

$$\Omega_\beta = \omega_\beta \frac{\mathrm{d}\tau}{\mathrm{d}t}, \tag{14}$$

where the redshift factor $\mathrm{d}\tau/\mathrm{d}t$ is determined from the conserved energy per unit mass, $\mathcal{E}$, and the g_{tt} component of the Kalb-Ramond BH metric as

$$\frac{\mathrm{d}t}{\mathrm{d}\tau} = -\frac{\mathcal{E}}{g_{tt}}. \tag{15}$$

In physical units, the angular frequencies of neutral test particles, as measured by a distant observer, are given by [102−104]:

$$\nu_i = \frac{1}{2\pi}\frac{c^3}{GM}\Omega_i[\mathrm{Hz}], \tag{16}$$

with $i \in \{r,\theta,\phi\}$, where Ω_r, Ω_θ, and Ω_ϕ denote the dimensionless radial, polar, and azimuthal angular frequencies in the observer's frame. In this work, all dynamical calculations are carried out in geometrized units with $M = 1$; thus, the evolution is expressed in units of the black-hole mass. The observable frequencies are then obtained through the standard inverse-mass scaling given in Eq. 16. In particular, the frequency profiles shown here correspond to a fiducial black-hole mass of $10\,M_\odot$; these dimensionless results can be directly rescaled for other masses. For the Kalb-Ramond BH coupled to nonlinear electrodynamics, these quantities are given explicitly by

$$\Omega_r^2 = \frac{e^{-2\eta}\left(-4\beta^2Q^4+9(\alpha-1)^2\beta e^{\eta}Q^2 r-(\alpha-1)^3 e^{2\eta}r^2(6\alpha+r-6)\right)}{(\alpha-1)^4 r^6}, \tag{17}$$

$$\Omega_\theta^2 = \frac{e^{-\eta}\left((\alpha-1)^2 e^{\eta} r-\beta Q^2\right)}{(\alpha-1)^2 r^4}, \tag{18}$$

$$\Omega_\phi^2 = \frac{e^{-\eta}\left((\alpha-1)^2 e^{\eta} r-\beta Q^2\right)}{(\alpha-1)^2 r^4}. \tag{19}$$

Fig. (9) illustrates the radial variation of ν_i for small-amplitude harmonic oscillations of neutral particles around a non-rotating Kalb–Ramond BH. The radial profiles of the azimuthal and polar frequencies coincide, reflecting the underlying spherical symmetry of the background spacetime. Variations in the BH parameters primarily shift the locations of the frequency maxima with respect to the event horizon, highlighting the quantitative impact of nonlinear electromagnetic contributions on the dynamics of orbiting test particles. In the same spirit as recent analyses of particle dynamics and perturbations in nonstandard black-hole backgrounds, our results show that the modified geometry affects not only orbital frequencies but also the nonlinear hydrodynamic variability of accreting matter [105]. Our epicyclic-frequency analysis is complementary to recent studies of particle dynamics and observational signatures in Kalb–Ramond black holes; here, we further link the underlying spacetime deformation directly to time-dependent BHL accretion and shock-cone variability [106].

V. NUMERICAL ANALYSIS OF ACCRETION FLOW AND VARIABILITY AROUND KALB-RAMOND BHS WITH NONLINEAR ELECTRODYNAMICS

In this section, we aim to perform a comprehensive

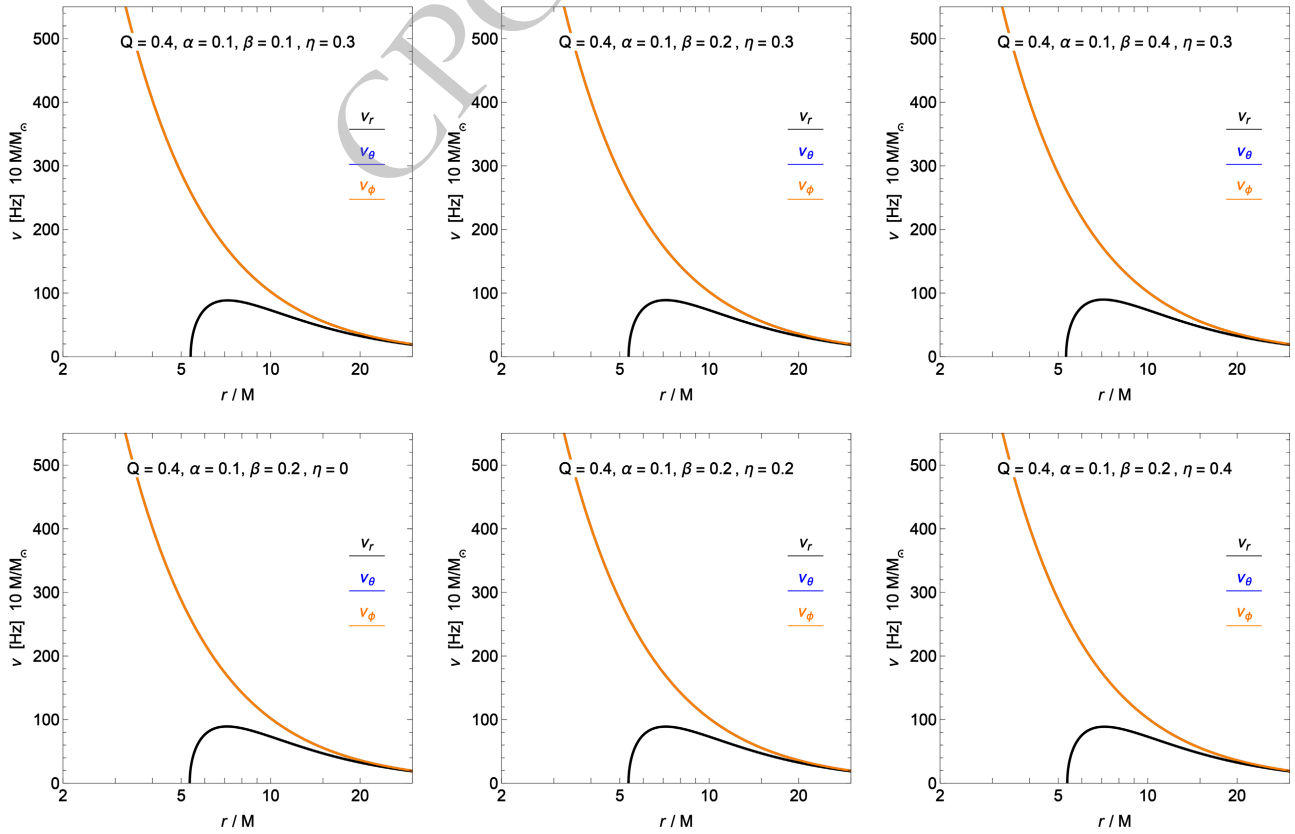

Fig. 9. (color online) Comparison of the radial and vertical epicyclic frequencies in the Kalb-Ramond BH spacetime. In the equatorial plane, the orbital (azimuthal) frequency coincides with the vertical frequency.

numerical simulation of accretion dynamics around Kalb-Ramond BHs coupled to nonlinear electrodynamics, in order to reveal how Lorentz symmetry breaking and nonlinear electromagnetic effects jointly influence the physical structure of spacetime and the resulting accretion flow. By numerically solving the GRH equations [107−110], possible new physical mechanisms that may arise due to spacetime deformation, their observational signatures, and the testability of gravity are investigated. To achieve this, a systematically adjusted set of spacetime parameter values, listed in Table 1, is employed in the simulations. By considering a broad and representative parameter range, the configurations summarized in Table I are constructed such that they simultaneously modify the event horizon of the BH and induce distinct levels of spacetime deformation within the Kalb-Ramond BH framework. In particular, the selected values of the parameters α, β, Q, and η allow us to systematically disentangle global geometric modifications driven by the Kalb-Ramond background from short-range corrections associated with nonlinear electrodynamics. On the other hand, the parameter Ξ defined in Table 1 is not a new spacetime parameter, but simply the effective charge strength defined by the combination of β, Q, and η. The parameter Ξ provides an effective measure of the nonlinear-electrodynamic contribution. In particular, this nonlinear-electrodynamic effect appears as a quantity that remains encoded in the spacetime geometry after being exponentially suppressed by η. In other words, β sets the intrinsic strength of the nonlinear electromagnetic sector, Q fixes the charge scale, and η weakens this contribution. Thus, the combination of these parameters through Ξ contains the net short-range correction relevant in the near-horizon region. Therefore, Ξ should be understood as a physically meaningful indicator of how strongly nonlinear electrodynamics competes with the global Kalb-Ramond deformation in determining the event-horizon-scale structure, the gravitational focusing of the flow, and the resulting shock-cone morphology. By varying the effective charge strength while keeping the BH mass fixed, a controlled comparison between the deformed spacetimes and the Schwarzschild case becomes possible. At the same time, this setup provides a consistent framework for isolating the influence of each deformation parameter on the accretion flow. This ensures that the numerical results reflect genuine spacetime effects, enabling a clear physical interpretation of the accretion morphology and variability in Kalb–Ramond BH spacetimes.

It is important to clarify the astrophysical validity of the parameter ranges listed in Table 1. The values adopted in Table 1 are not intended as direct best-fit constraints from current Event Horizon Telescope (EHT) or gravitational-wave observations. Rather, these parameters are chosen to reveal how the physical mechanisms developing around the black hole depend on the deformation introduced by the spacetime parameters. Current observational results mainly constrain how much the black-hole spacetime can deviate from the Kerr or Schwarzschild cases, rather than uniquely determining the individual values of α, β, Q, and η. In particular, EHT analyses of Sagittarius A* have shown that the observed horizon-scale image is broadly consistent with the Kerr case [111]. On the other hand, recent results from LIGO-Virgo-KAGRA in the inspiral, merger, and ringdown regimes indicate no significant deviation from general relativity [112]. From this perspective, the weakly modified models C1 and C2 can be regarded as having spacetime geometries that are more consistent with current observations. In contrast, the more strongly deformed models C3-C6 are included to reveal the limiting response of the shock-cone structure, stagnation-point location, and variability properties under larger departures from the standard geometry. Therefore, the spacetime parameters listed in Table 1 include both near-GR models that are more compatible with current observations and strongly deformed models that may be useful for exploring configurations that could become observationally relevant in the future.

Here, we also clarify the validity of the numerical method employed in this work. In the BHL simulations

Table 1. We employ models to constrain the deformation parameters of Kalb-Ramond black holes with nonlinear electrodynamics using BHL accretion simulations. The parameters α, β, Q, and η govern the global spacetime deformation and the short-range $1/r^2$ corrections to the gravitational potential. The effective charge strength is defined as $\Xi \equiv \beta Q^2 e^{-\eta}$. All models assume $M = 1$ and admit a real event horizon of radius r_h.

Model	α	β	$Q(M)$	η	$\Xi = \beta Q^2 e^{-\eta}(M^2)$	$r_h(M)$
C1	0.00	1.00	0.80	0.50	0.3880	1.7822
C2	0.10	1.00	0.70	0.20	0.4008	1.5035
C3	0.30	0.20	0.60	0.40	0.0483	1.3482
C4	0.20	1.20	0.70	0.60	0.4610	1.2864
C5	0.30	2.00	0.60	1.00	0.2649	1.0341
C6	0.40	3.00	0.50	1.40	0.1542	0.8275

presented in this study, the time evolution of the fluid accreting onto the black hole is obtained on a fixed Kalb-Ramond background metric. Therefore, the self-gravity that could be generated by the accreting matter is neglected. This is justified because the present work is focused only on the physical processes occurring in the region close to the black hole, namely where the gravitational field is very strong. In this region, the gravitational timescale is much shorter than the self-gravity timescale, which allows this effect to be safely neglected. For this reason, the models considered in this work should be interpreted within the test-fluid approximation. In other words, the flow probes the deformed spacetime geometry without dynamically modifying it. In this framework, the effective charge-strength parameter Ξ measures the magnitude of the short-range nonlinear electromagnetic corrections already encoded in the background geometry. However, by itself, it does not imply a breakdown of the test-fluid approximation. Such a breakdown would require the mass-energy of the accreting fluid in the strong-field region to become non-negligible compared with the black-hole mass. As a result, our findings are reliable because they describe the system in a regime where the effect of the internal forces of the fluid on the spacetime geometry remains sufficiently small to be neglected. Therefore, the changes observed in the dynamical structure of the shock cone should be understood as consequences of the spacetime deformation.

Understanding how the structure of the shock cone formed around a BH in BHL accretion varies with spacetime parameters is crucial. Such variations reveal how deformations in the spacetime geometry affect the redistribution of matter around the BH and modify the momentum and energy of the accreting material in the strong-field regime, thereby informing the interpretation of observable signatures. Variations in the cone geometry—namely its opening angle and the density of matter trapped within —directly affect the mass accretion rate, which in turn alters the stability properties of the shock cone. Consequently, nonlinear electrodynamics and modified gravity may yield observationally distinguishable outcomes. In this context, we model the shock-cone structure formed through the BHL accretion mechanism around Kalb-Ramond BHs coupled to nonlinear electrodynamics for the configurations listed in Table 1, and the influence of the spacetime parameters α, β, Q, and η is illustrated in Fig. 10. Compared with the Schwarzschild solution shown in the upper-left panel of Fig. 10, all Kalb-Ramond models systematically exhibit pronounced changes in both the geometry of the shock cone and the distribution of rest-mass density inside and outside the cone. These differences arise from spacetime deformations induced by Lorentz-symmetry breaking and nonlinear electrodynamics.

For the C2 model shown in Fig. 10, where the deformation parameters are relatively weak, the shock cone remains wide, similar to the Schwarzschild case, while the location of the maximum density inside the cone shifts closer to the BH. The density gradients remain smooth, indicating a moderate level of spacetime deformation. In the C3 model, the opening angle of the cone becomes noticeably narrower and the structure appears more elongated. In particular, the contour lines of rest-mass density near the stagnation point are significantly compressed, indicating strong flow focusing and an enhanced density contrast. Compared to C3, the C4 model shows a slight re-expansion of the cone opening angle, accompanied by asymmetrically distributed density contours, signaling competing effects of global geometric deformation and nonlinear electromagnetic corrections. In the C5 model, the shock cone becomes strongly compressed and the high-density region moves closer to the BH horizon, consistent with the combined influence of Kalb-Ramond deformation and nonlinear electrodynamics. The steep density gradients indicate strong gravitational focusing. Finally, among all models, C6 exhibits the most pronounced deviation from the Schwarzschild case, with the dense region inside the cone confined even closer to the BH horizon. We emphasize, however, that the strong compression observed in models C5 and C6 is not driven by the largest values of the effective charge strength Ξ. According to Table 1, Ξ is 0.2649 for C5 and 0.1542 for C6, whereas larger values are found in models C1, C2, and C4. This indicates that the pronounced narrowing of the shock cone in C5 and C6 is primarily associated with cumulative spacetime deformation — particularly the larger values of α and the corresponding reduction of the event-horizon radius—rather than with a maximization of Ξ alone.

Fig. 11 illustrates the azimuthal variation of the rest-mass density at $r = 2.66M$ for the Schwarzschild case and the Kalb-Ramond BH models listed in Table 1. This directly demonstrates how the spacetime parameters modify the structure of the shock cone formed around the BH. As the Lorentz-symmetry-breaking parameter α increases, the maximum density inside the cone systematically decreases, indicating that the Kalb-Ramond background weakens the compression efficiency of matter accreting toward the BH. The reduction in peak amplitude indicates that the matter distribution around the BH is reorganized by the altered spacetime geometry. The deformed spacetime geometry effectively weakens the gravitational field, which in turn hinders efficient compression of matter inside the cone. At the same time, as the effective charge parameter Ξ, which is controlled by β, Q, and η, decreases, a significant reduction in the opening angle of the shock cone is observed. These nonlinear electromagnetic corrections enhance short-range repulsive effects, modify the balance between gravitational focusing and pressure-supported forces, and consequently reconfigure

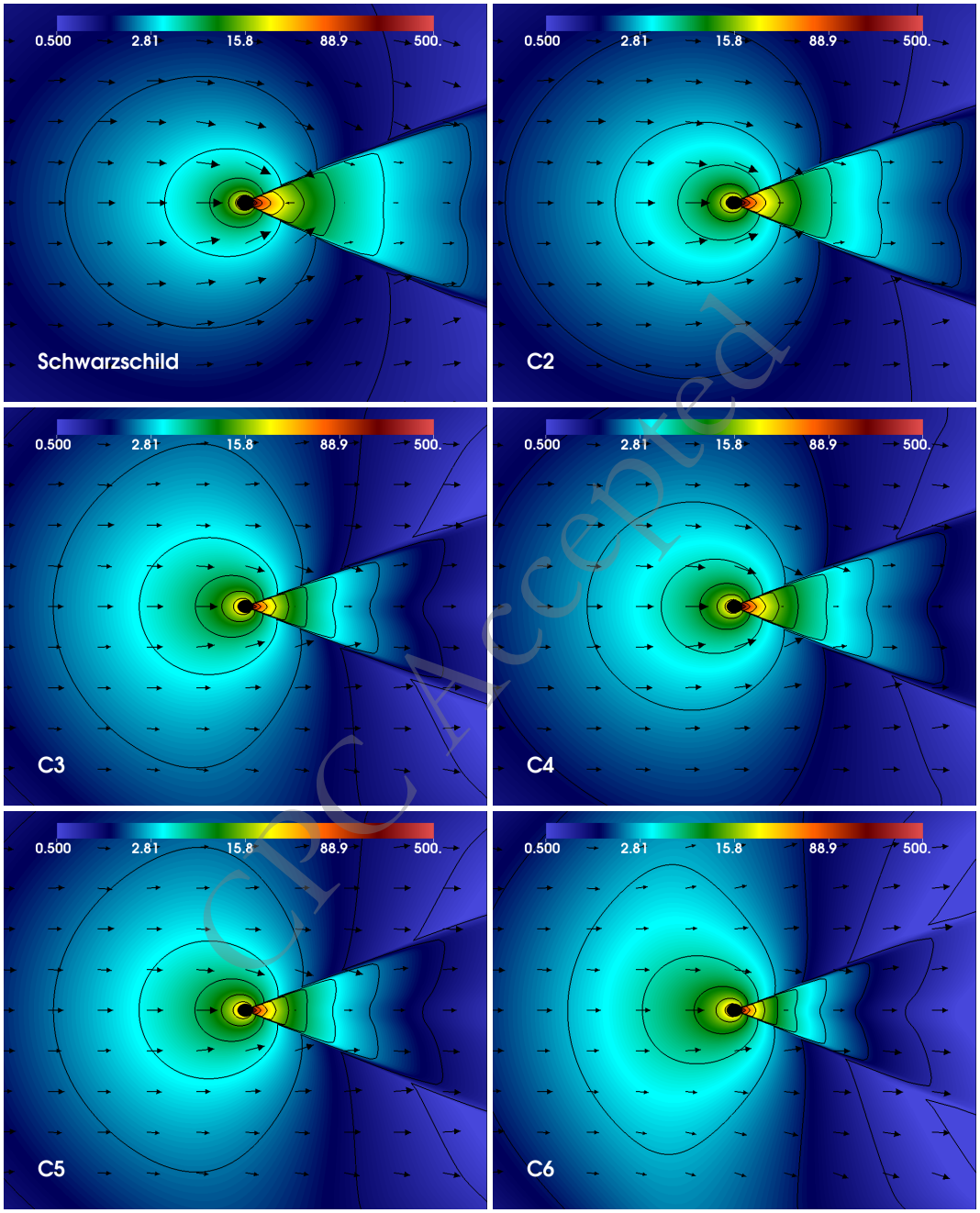

Fig. 10. (color online) The dynamical structure of the shock cone formed by the BHL accretion mechanism around the Schwarzschild and Kalb-Ramond BH models listed in Table 1 is illustrated with color maps and contour plots of the rest-mass density. Vector fields are overlaid on the density distribution to show how matter accretes toward the BH and how the shock cone develops in the downstream region opposite the accretion flow. Each snapshot depicts the late-time, steady-state configuration of the system.

the cone geometry.

From an observational perspective, both behaviors of the shock cone have a direct impact on QPOs. A lower peak density reduces heating within the shock cone and decreases the local emissivity. In addition, as the opening angle becomes smaller, the coherence and characteristic size of the post-shock region are modified. This can either completely suppress strong oscillations or, if they persist, shift their characteristic frequencies, as will be discussed later. As a result, the decrease in peak density with increasing α, together with the influence of the effective charge parameter, causes significant changes in the power spectral density (PSD). These effects establish a clear connection between spacetime-deformation parameters in Kalb-Ramond BHs coupled to nonlinear electrodynamics and observable QPO signatures. Consequently, the azimuthal density profile emerges as a sensitive diagnostic of modified-gravity effects in the

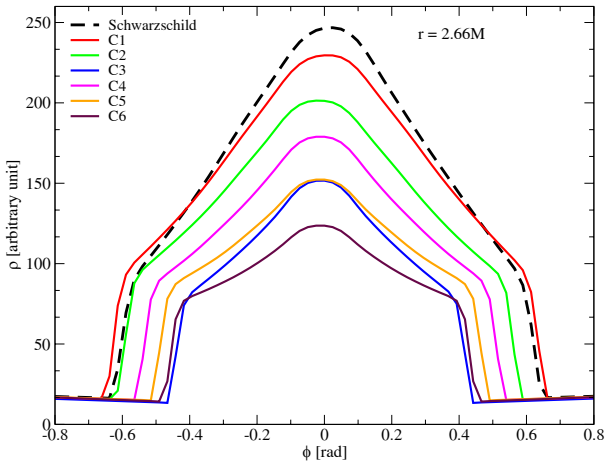

Fig. 11. The azimuthal variation of the rest-mass density at $r = 2.66M$ is shown for the Schwarzschild case and for various Kalb-Ramond BH models. This illustrates the density distribution of matter both inside and outside the shock cone. It clearly demonstrates that spacetime parameters modify the gravitational field, leading to significant changes in the structure of the resulting shock cone.

strong-field accretion region.

The stagnation point is the location inside the shock cone where the accreting matter becomes momentarily stationary. From this point, the material closer to the BH is funneled inward within the cone toward the event horizon, while the matter outside the cone is redirected outward. Therefore, the stagnation point directly reflects the effectiveness of gravitational focusing acting on the accretion flow. As shown in the upper panel of Fig. 12, the stagnation point varies systematically across the different models. With an increasing Lorentz symmetry-breaking parameter α, the stagnation point moves closer to the BH horizon, indicating a reduction in gravitational focusing. This, in turn, implies a gradual decrease in the size of the shock cone and consequently in the effective cavity formed downstream of the accretor. The evolution of the stagnation point is fully consistent with the changes in the shock-cone structures shown in Figs. 10 and 11. As seen in the upper panel of Fig. 12, in the C4 model, the value of α is lower than in C3, and accordingly the stagnation point shifts slightly away from the BH. This behavior signifies a partial recovery of gravitational focusing. Overall, this trend illustrates the non-monotonic response of the accretion flow to competing geometric deformation and nonlinear electrodynamic effects, and demonstrates that the stagnation radius provides a consistent link between flow morphology, density stratification, and the dynamical properties of accretion in Kalb-Ramond BH spacetimes.

The middle panel of Fig. 12 shows how the shock-cone opening angle $\Delta\varphi$ varies across the different models. This opening angle measures how efficiently matter ac-

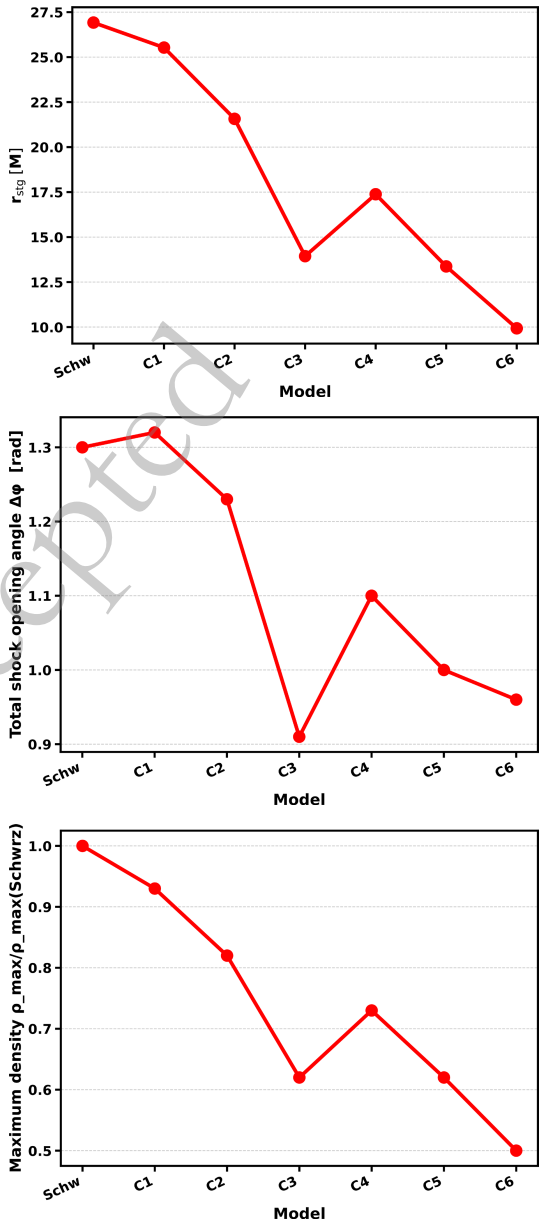

Fig. 12. (color online) Variations in the stagnation-point location, the shock-cone opening angle, and the maximum rest-mass density of matter trapped inside the shock cone are shown for the different models. These trends, plotted for the Schwarzschild and Kalb-Ramond BH configurations, demonstrate how modifications to the spacetime systematically alter the geometry and density structure of the shock cone, as well as the overall accretion dynamics.

creting toward the BH through the BHL mechanism is focused, and thus reflects the strength of gravitational focusing. It also encodes the combined influence of spacetime deformation parameters and nonlinear electrodynamic effects. As seen in the figure, $\Delta\varphi$ generally decreases as one moves away from the Schwarzschild case toward Kalb-Ramond BH models with stronger deformation. This indicates that increasing spacetime deforma-

tion leads to a more collimated shock cone and a progressively smaller post-shock cavity. Such behavior directly affects the oscillation modes trapped inside the cavity and results in shifts in their characteristic frequencies. These trends are fully consistent with the flow morphology and density distributions shown in Figs. 10 and 11. However, the decrease in $\Delta\varphi$ is not observed in the C1 and C4 models, where the opening angle is larger than that of their neighboring configurations. This non-monotonic behavior arises from the combined effect of the nonlinear electrodynamic parameters β, Q, and η. The strength of this combined effect for each model is quantified by the parameter Ξ, as listed in Table I. As seen in Table 1, whenever Ξ attains relatively large values, as in the C1 and C4 models, short-range nonlinear electrodynamic corrections significantly modify the balance between gravitational focusing and pressure-supported forces in the post-shock region, leading to an increase in $\Delta\varphi$. In these models, the strong effective charge partially counteracts the focusing tendency triggered by the Kalb-Ramond deformation parameter α, causing a re-expansion of the shock-cone opening angle. Consequently, the behavior of $\Delta\varphi$ reflects a competition between global spacetime deformation effects, which favor narrower cones, and nonlinear electrodynamic corrections encoded in Ξ, which contribute to widening the opening angle.

The bottom panel of Fig. 12 shows the variation of the maximum density of matter trapped inside the shock cone as a function of the model. The behavior of the maximum density closely follows that of the stagnation point shown in the upper panel. As listed in Table 1, the spacetime deformation parameter α increases with model number. As α increases, the maximum density decreases, mirroring the inward shift of the stagnation point. Only in the C4 model does the maximum density tend to increase again, because the value of α in C4 is smaller than in C3. As the stagnation point approaches the BH horizon, a larger fraction of matter inside the shock cone is redirected outward, which leads to a reduction in the maximum density.

Fig.13 shows the mass accretion rate in the strong-field regime for the Schwarzschild and Kalb-Ramond BH models. As seen in the figure, both the magnitude of the mass accretion rate and its oscillatory characteristics exhibit significant changes, particularly in the Kalb-Ramond models. This demonstrates how the dynamical response of BHL accretion is governed by the underlying spacetime deformation. In the Schwarzschild case and in the weakly deformed Kalb-Ramond models C1 and C2, the shock-cone opening angle remains relatively wide, and the cavity in the post-shock region between the stagnation point and the BH horizon is large because the stagnation point lies sufficiently far from the horizon. In this regime, the mass accretion rate displays coherent flow instabilities, giving rise to pronounced oscillations. The

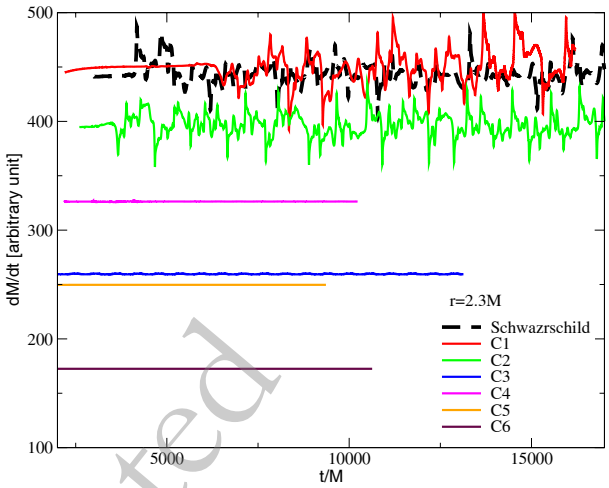

Fig. 13. (color online) The time evolution of the mass accretion rate measured at $r = 2.3M$ is presented for the Schwarzschild case and the Kalb-Ramond BH models listed in Table 1. The Schwarzschild, C1, and C2 models clearly exhibit oscillatory behavior once the system has reached a steady state, whereas the strongly deformed Kalb-Ramond models display a smoother, nearly steady accretion rate.

time-dependent fluctuations originate from the interaction between gravitational focusing and pressure-supported oscillations of the shock cone. These oscillations maintain a finite amplitude as long as the stagnation point remains sufficiently distant from the BH horizon. In contrast, for the strongly deformed Kalb-Ramond models C3-C6, the stagnation point moves closer to the BH horizon, leading to an increasingly collimated shock cone. As a result, a substantial fraction of the inflowing matter rapidly falls through the horizon, suppressing large-scale oscillatory modes and producing a smoother accretion rate. As discussed in detail earlier, larger values of the deformation parameter α cause the cavity within the post-shock region to shrink, while nonlinear electromagnetic effects further enhance the outward damping of fluctuations. Observationally, whereas the Schwarzschild, C1, and C2 cases can generate detectable temporal signatures and QPOs, the remaining Kalb-Ramond models make QPO detection nearly impossible.

The PSDs computed from the mass accretion rate for the Schwarzschild, C1, and C2 models exhibit clear differences, as shown in Fig.14. These differences arise from the spacetime deformation induced by the Kalb-Ramond parameters. In the Schwarzschild case, the PSD shows broadband variability with modest peaks corresponding to the natural oscillation modes of the shock cone, supported by gravitational focusing within the post-shock cavity. In contrast, the weakly modified Kalb-Ramond models C1 and C2 produce stronger, sharper peaks, indicating enhanced QPO-like behavior. Moreover, the QPO frequencies in C1 and C2 are shifted relative to the

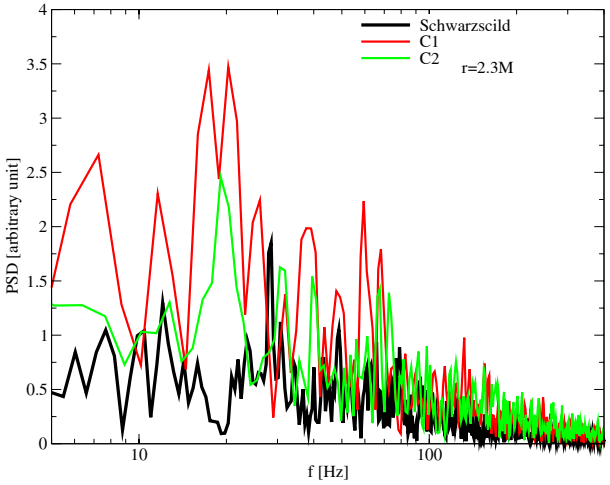

Fig. 14. (color online) Power spectral densities (PSDs) computed from the mass accretion rate at $r = 2.3M$ are shown for the Schwarzschild, C1, and C2 models, assuming a black hole mass of $M = 10\,M_{\odot}$. The weakly deformed Kalb-Ramond models C1 and C2 produce stronger and more coherent shifted peaks than the Schwarzschild model.

Schwarzschild case, with the low-frequency QPOs further amplified. This behavior arises because, in C1 and C2, the stagnation point remains sufficiently far from the BH horizon, allowing strong oscillations to persist; at the same time, dynamical modifications of the shock-cone structure shift the characteristic QPO frequencies. The peaks in the Kalb-Ramond cases also appear more coherent. In the remaining, more strongly deformed Kalb-Ramond models, however, the spacetime deformation highly collimates the accretion flow, and oscillations, especially in the post-shock region, are strongly suppressed. As a result, the accretion rate exhibits smoother temporal behavior, and no QPOs form in these models.

To quantify this, we also computed PSDs for the strongly deformed models C3-C6. In these analyses, no distinct narrow peak emerges above the irregular amplitudes produced by noise. The remaining variability can therefore be interpreted only as an upper bound on any possible QPO-like signal, rather than as a resolved oscillation mode. In all of these models, the residual amplitudes are much smaller than the dominant QPO peaks clearly seen in C1 and C2, indicating that strong spacetime deformation significantly suppresses the coherent peaks produced by shock-cone oscillations, rendering them indistinguishable from the residual fluctuations.

Conversely, the PSDs presented here are computed solely from the time variability of the mass accretion rate. Although they suggest a plausible physical mechanism for sources producing QPOs within a certain frequency range, they cannot be used for a direct one-to-one comparison with observations to determine instrumental detection thresholds. Such a comparison would require numerically computed observables based on radiation transport, which are beyond the scope of the present paper.

VI. CONCLUSIONS

In this paper, we investigate neutral test particle dynamics in the static KR BH model coupled to nonlinear electrodynamics, analyzing the effective potential, circular orbits, ISCOs, and general particle trajectories. Also, the geodesic motion is derived using the Hamiltonian approach, which allows explicit separation of the radial and angular components and incorporates conserved quantities, specifically the energy $\mathcal{E}$ and azimuthal angular momentum $\mathcal{L}$, associated with the spacetime Killing vectors. In this case, the effective potential $V_{\rm eff}(r)$, encompassing both gravitational and nonlinear electromagnetic contributions, governs the radial motion and orbital stability. Focusing on the equatorial plane, we obtain analytic expressions for the energy and angular momentum of circular orbits, which fully account for the nonlinear electromagnetic effects through the BH charge Q and the exponential nonlinear factor $e^{-\eta}$. These results indicate that increasing either the BH charge or the orbital angular momentum deepens the effective potential, enabling tighter and more stable orbits nearer to the horizon, whereas reducing Q or $\mathcal{L}$ decreasing the gravitational binding results in wider orbits. The ISCO, determined from the conditions $V'_{\rm eff} = V''_{\rm eff} = 0$, shifts outward as the BH charge increases, reflecting the competition between gravitational attraction and electromagnetic repulsion. Also, numerical integration of the geodesic equations confirms these behaviors, showing that higher Q extends the radial domain of stable motion and modifies orbital geometries relative to the uncharged configuration. In the limit where the nonlinear electrodynamics parameters vanish and the KR charge $\alpha \to 0$, the metric function reduces to the classical Schwarzschild BH form $f(r) \to 1 - 2M/r$, and the effective potential, circular orbit parameters, and ISCO radius reproduce the standard Schwarzschild values, including the innermost stable orbit at $r = 3r_g$. In the further limit $M \to 0$, the gravitational contribution disappears, yielding $\mathcal{V}_{\rm eff} \to 1 + \mathcal{L}^2/r^2$, corresponding to Minkowski spacetime, where only the centrifugal term governs the dynamics and no gravitational binding exists. In this context, these limiting cases demonstrate that the deviations observed in KR BHs with nonlinear electrodynamics constitute quantitative modifications of orbital properties relative to the Schwarzschild BH solution, affecting the depth, curvature, and stability of the potential well, the energy and angular momentum of circular orbits, and ISCO positions, while the classical Schwarzschild behavior is exactly recovered when the KR and nonlinear electromagnetic contributions are removed.

The analysis of small perturbations around stable circular orbits in the equatorial plane of a non-rotating Kalb-

Ramond BH coupled to nonlinear electrodynamics enables a quantitative characterization of epicyclic motion and its dependence on the spacetime geometry and gauge sector. By representing radial, vertical, and azimuthal deviations as linear harmonic oscillations around equilibrium orbits, the corresponding angular frequencies ω_r, ω_θ, and ω_ϕ, as measured by a local comoving observer, are obtained from the second derivatives of the effective potential $V_{\rm eff}(r,\theta)$. These expressions explicitly incorporate the contributions of the Kalb-Ramond parameter α, the nonlinear electromagnetic coupling βQ^2, and the metric function e^{η}, testing direct insight into how each component modifies particle dynamics. Analysis indicates that the radial frequency ω_r exhibits the largest sensitivity to the combined influence of the gravitational and nonlinear electromagnetic potentials, producing shifts in both the magnitude and radial position of frequency maxima relative to the Schwarzschild reference, whereas the vertical and azimuthal frequencies remain identical in the equatorial plane, $\omega_\theta = \omega_\phi$, reflecting the residual spherical symmetry of the background. Also, transforming these frequencies to those measured by a distant static observer, Ω_r, Ω_θ, and Ω_ϕ, requires the gravitational redshift factor $\mathrm{d}\tau/\mathrm{d}t$ associated with the conserved energy per unit mass $\mathcal{E}$, yielding observable frequency relations that incorporate both spacetime curvature and gauge field effects.

Radial profiles show that nonlinear electromagnetic interactions and the Kalb-Ramond field systematically alter the epicyclic frequencies, with stronger deviations at smaller orbital radii, while the equality of polar and azimuthal frequencies persists, confirming spherical symmetry. In this case, in the limit $\alpha \to 1$ and $\beta Q^2 \to 0$, corresponding to the absence of Kalb-Ramond and nonlinear electromagnetic contributions, the epicyclic frequencies consistently recover the Schwarzschild values for neutral particles, providing a consistency check and illustrating that additional fields generate measurable corrections to orbital dynamics. Also, these modifications are reflected as shifts in the frequency maxima positions relative to the Schwarzschild event horizon, changes in the relative magnitudes of radial and azimuthal oscillations, and potential adjustments in resonance conditions relevant for QPOs in accretion disks, emphasizing the observational significance of the Kalb-Ramond and nonlinear electromagnetic parameters. In this context, these results establish a framework to quantify how extensions of GR, incorporating antisymmetric tensor fields and nonlinear gauge interactions, influence the harmonic motion of neutral test particles and their observable epicyclic frequencies, while recovering classical Schwarzschild behavior under appropriate limits.

In the numerical simulations section of this work, we investigated the effects of spacetime deformation parameters around Kalb-Ramond BHs on accretion flow dynamics by numerically modeling the infall of matter toward the BH through the BHL accretion mechanism. Using the systematically varied parameters listed in Table 1, we demonstrate that the shock-cone morphology undergoes significant changes, the stagnation point inside the cone moves progressively closer to the BH horizon with increasing α, the shock opening angle gradually decreases, and as a consequence, the maximum density of matter trapped inside the cone is reduced. At the same time, we showed that an increase in effective charge strength $\Xi \equiv \beta Q^2 e^{-\eta}$ leads, in particular, to an increasing tendency in both shock opening angle and stagnation point location. These behaviors indicate the emergence of a coherent physical picture in which Lorentz symmetry breaking and nonlinear electrodynamic corrections weaken gravitational focusing and reduce the size of the cavity formed in the post-shock region.

In addition, the time-dependent behavior of the accretion flow reveals the dynamical consequences of spacetime deformation. For the Schwarzschild case and the weakly deformed Kalb-Ramond models C1 and C2, pronounced QPOs in the mass accretion rate are observed, and the corresponding PSD analyses show clear QPO frequencies. Due to the deformed spacetime geometry, these QPO frequencies are shifted, and even higher-amplitude peaks with enhanced observational relevance emerge. On the other hand, in Kalb-Ramond models with strong deformation parameters, these oscillations are systematically suppressed, resulting in a smooth and nearly steady accretion regime. The numerical results demonstrate a direct connection between the shock-cone geometry, the stagnation point, and the variability properties. Consequently, the observability and testability of Kalb-Ramond BHs are shown to be strongly dependent on the spacetime geometry and its deformation parameters.

ACKNOWLEDGMENTS

All numerical simulations were performed on the Phoenix High-Performance Computing facility at the American University of the Middle East (AUM) in Kuwait.

DATA AVAILABILITY STATEMENT

The datasets generated and analyzed in this study were produced using high-performance computing resources. These data are not publicly available due to their large size and computational nature; however, they are available from the corresponding author upon reasonable request.

References

[1] M. Kalb and P. Ramond, Phys. Rev. D **9**, 2273 (1974)
[2] B. Mukhopadhyaya, S. Sen, and S. SenGupta, Phys. Rev. D **70**, 066009 (2004)
[3] E. L. Junior *et al*., Phys. Rev. D **110**, 024077 (2024)
[4] J. Erdmenger, R. Meyer, and J. P. Shock, JHEP **2007**, 091 (2007)
[5] L. A. Lessa, J. E. G. Silva, R. V. Maluf, and C. A. S. Almeida, Eur. Phys. J. C **80**, 1 (2020)
[6] E. Elizalde, S. D. Odintsov, V. K. Oikonomou, and T. Paul, JCAP **2019**, 017 (2019)
[7] S. J. Rey, Phys. Rev. D **40**, 3396 (1989)
[8] V. A. Kostelecký, Phys. Rev. D **69**, 105009 (2004)
[9] R. bbluhm and V. A. Kostelecký, Phys. Rev. D **71**, 065008 (2005)
[10] R. V. Maluf, J. E. G. Silva, and C. A. S. Almeida, Phys. Lett. B **749**, 304 (2015)
[11] W. Yu, M. van der Klis, and R. Fender, arXiv: astro-ph/0207645 (2002).
[12] A. Al-Badawi, F. Ahmed, and İ. Sakallı, Phys. Dark Univ. 102076 (2025)
[13] M. van Doesburgh and M. van der Klis, Mon. Not. R. Astron. Soc. **490**, 5270 (2019)
[14] C. Zhang and D. Wang, IAU Symp. **290**, 381 (2013), arXiv: 1305.2803
[15] İ. Sakallı, E. Sucu, A. Al-Badawi, and F. Ahmed, arXiv: 2512.18881 (2025).
[16] F. Ahmed, A. Al-Badawi, İ. Sakallı, and S. Shaymatov, Chin. J. Phys. **96**, 770 (2025)
[17] E. Sucu, İ. Sakallı, and Y. Sucu, Int. J. Geom. Methods Mod. Phys. 2650116 (2026)
[18] A. Al-Badawi, F. Ahmed, O. Donmez, F. Dogan, B. Pourhassan, i. Sakallı, and Y. Sekhmani, Phys. Dark Univ. **51**, 102206 (2026), arXiv: 2509.08674
[19] O. Dönmez, O. Zanotti, and L. Rezzolla, Mon. Not. R. Astron. Soc. **412**, 1659 (2011)
[20] O. Donmez, Eur. Phys. J. C **84**, 524 (2024)
[21] A. Ashraf, O. Donmez, A. Bouzenada, C. Yuan, A. Caliskan, G. Rakhimova, and A. Abdujabbarov, arXiv: 2602.05747 (2026).
[22] O. Donmez, arXiv: 2503.16665 (2025).
[23] D. Capelo and J. Páramos, Phys. Rev. D **91**, 104007 (2015)
[24] R. Casana, A. Cavalcante, F. P. Poulis, and E. B. Santos, Phys. Rev. D **97**, 104001 (2018)
[25] O. bbertolami and J. Páramos, Phys. Rev. D **72**, 044001 (2005)
[26] A. Övgün, K. Jusufi, and İ. Sakallı, Phys. Rev. D **99**, 024042 (2019)
[27] R. Oliveira, D. M. Dantas, V. Santos, and C. A. S. Almeida, Class. Quantum Grav. **36**, 105013 (2019)
[28] C. Ding, C. Liu, R. Casana, and A. Cavalcante, Eur. Phys. J. C **80**, 178 (2020)
[29] Z. Li and A. Övgün, Phys. Rev. D **101**, 024040 (2020)
[30] B. Altschul, Q. G. Bailey, and V. A. Kostelecký, Phys. Rev. D **81**, 065028 (2010)
[31] R. V. Maluf, A. A. Araújo Filho, W. T. Cruz, and C. A. S. Almeida, EPL **124**, 61001 (2018)
[32] W. F. Kao, W. B. Dai, S. Y. Wang, T. K. Chyi, and S. Y. Lin, Phys. Rev. D **53**, 2244 (1996)
[33] H. Reissner, Ann. Phys. **50**, 106 (1916)
[34] G. Nordström, Proc. Kon. Ned. Akad. **20**, 1238 (1918)
[35] R. M. Wald, *General Relativity* (University of Chicago Press, Chicago, 1984).
[36] B. Gupta and P. Singh, Phys. Rev. D **89**, 063520 (2014)
[37] T. K. Dey, S. Mukherji, S. Mukhopadhyay, and S. Sarkar, JHEP **0704**, 014 (2007)
[38] K. Srinivasan and T. Padmanabhan, Phys. Rev. D **60**, 024007 (1999)
[39] M. Angheben, M. Nadalini, L. Vanzo, and S. Zerbini, JHEP **05**, 014 (2005)
[40] A. Al-Badawi, F. Ahmed, and İzzet Sakallı, Physics of the Dark Universe **50**, 102076 (2025)
[41] R. Kerner and R. B. Mann, Phys. Rev. D **73**, 104010 (2006)
[42] P. Mitra, Phys. Lett. B **648**, 240 (2007)
[43] E. T. Akhmedov, V. Akhmedova, and D. Singleton, Phys. Lett. B **642**, 124 (2006)
[44] S. Kanzi and İ. Sakallı, Nucl. Phys. B **946**, 114703 (2019)
[45] I. Nishonov, S. Murodov, B. Ahmedov, S. U. Khan, J. Rayimbaev, I. Ibragimov, and S. Sabirov, Eur. Phys. J. C **85**, 1029 (2025)
[46] S. U. Khan, M. Shahzadi, and J. Ren, Phys. Dark Universe **26**, 100331 (2019)
[47] S. U. Khan and J. Ren, Phys. Dark Universe **30**, 100644 (2020)
[48] B. Rahmatov, M. Zahid, S. U. Khan, J. Rayimbaev, I. Ibragimov, Z. Yuldoshev, A. Dauletov, and S. Muminov, Chin. Phys. C **49**, 075105 (2025)
[49] S. U. Khan, J. Rayimbaev, Y. Turaev, O. Sirajiddin, S. Usanov, and W. Wang, Eur. Phys. J. C **86**, 207 (2026)
[50] A. Ditta *et al*., Phys. Dark Universe **46**, 101573 (2024)
[51] G. Mustafa *et al*., Phys. Dark Universe **47**, 101753 (2025)
[52] G. Mustafa *et al*., Phys. Dark Universe **47**, 101765 (2025)
[53] J. Rayimbaev, P. Tadjimuratov, A. Abdujabbarov, B. Ahmedov, and M. Khudoyberdieva, Galaxies **9**, 75 (2021)
[54] S. Jumaniyozov, S. U. Khan, J. Rayimbaev, A. Abdujabbarov, S. Urinbaev, and S. Murodov, Eur. Phys. J. C **84**, 964 (2024)
[55] S. Faraji, Astron. Rep. **67**, S207 (2023)
[56] Z. Stuchlík and J. Vrba, JCAP **11**, 059 (2021)
[57] J. Homan *et al*., Astrophys. J. **586**, 1262 (2003)
[58] J. Rayimbaev, B. Ahmedov, and A. H. Bokhari, Int. J. Mod. Phys. D **31**, 2240004 (2022)
[59] A. Ditta *et al*., Phys. Dark Universe **47**, 101818 (2025)
[60] A. Ditta *et al*., J. High Energy Astrophys. **45**, 62 (2025)
[61] M. Qi, J. Rayimbaev, and B. Ahmedov, Eur. Phys. J. C **83**, 730 (2023)
[62] L. Rezzolla and O. Zanotti, *Relativistic Hydrodynamics* (Oxford University Press, Oxford, 2013).
[63] A. Ashraf *et al*., Nucl. Phys. B **1014**, 116873 (2025)
[64] A. Ashraf *et al*., Phys. Dark Universe **47**, 101787 (2025)
[65] R. Narayan, I.-s. Yi, and R. Mahadevan, Astron. Astrophys. Suppl. Ser. **120**, 287 (1996), arXiv: astro-ph/9509140
[66] A. Ashraf *et al*., Phys. Dark Universe **47**, 101725 (2025)
[67] A. Ashraf *et al*., Phys. Dark Universe **47**, 101823 (2025)
[68] L. Rezzolla, S. Yoshida, T. J. Maccarone, and O. Zanotti, Mon. Not. R. Astron. Soc. **344**, L37 (2003)
[69] G. Török, A. Kotrlová, E. Šrámková, and Z. Stuchlík, Astron. Astrophys. **531**, A59 (2011)
[70] A. Ashraf *et al*., Phys. Dark Universe **48**, 101836 (2025)
[71] A. Saleem *et al*., Nucl. Phys. B **1017**, 116926 (2025)
[72] Z. Stuchlík, A. Kotrlová, and G. Török, Astron. Astrophys. **525**, A82 (2011)

[73] Z. Stuchlík, A. Kotrlová, and G. Török, Astron. Astrophys. **552**, A10 (2013)
[74] A. Bouzenada *et al*., Nucl. Phys. B **1017**, 116928 (2025)
[75] G. Mustafa, I. Hussain, and W.-M. Liu, Chin. J. Phys. **80**, 148 (2022)
[76] X. Jiang, P. Wang, H. Yang, and H. Wu, Eur. Phys. J. C **81**, 1043 (2021)
[77] L. Amarilla, E. F. Eiroa, and G. Giribet, Phys. Rev. D **81**, 124045 (2010)
[78] Y. Liu, G. Mustafa, S. K. Maurya, and F. Javed, Eur. Phys. J. C **83**, 584 (2023)
[79] A. Ashraf *et al*., Eur. Phys. J. C **85**, 383 (2025)
[80] S. K. Maurya *et al*., Nucl. Phys. B **1020**, 117139 (2025)
[81] Z. Stuchlík and M. Kološ, Astron. Astrophys. **586**, A130 (2016)
[82] R. A. Remillard *et al*., Astrophys. J. Lett. **517**, L127 (1999)
[83] E. H. Morgan, R. A. Remillard, and J. Greiner, Astrophys. J. **482**, 993 (1997)
[84] R. A. Remillard *et al*., Astrophys. J. **637**, 1002 (2006)
[85] A. Ditta *et al*., Nucl. Phys. B **1019**, 117099 (2025)
[86] A. Ashraf *et al*., Phys. Dark Universe **48**, 101874 (2025)
[87] M. Shahzadi, M. Kološ, R. Saleem, and Z. Stuchlík, Class. Quantum Grav. **41**, 075014 (2024)
[88] S. Jumaniyozov *et al*., Eur. Phys. J. C **85**, 126 (2025)
[89] O. Dönmez, Eur. Phys. J. C **84**, 524 (2024)
[90] A. Ditta *et al*., Nucl. Phys. B **1018**, 117059 (2025)
[91] A. Bouzenada *et al*., Phys. Dark Universe **51**, 102216 (2025)
[92] A. Garg, R. Misra, and S. Sen, Mon. Not. R. Astron. Soc. **514**, 3285 (2022)
[93] M. Masterson *et al*., Nature **638**, 370 (2025)
[94] C. Bambi, JCAP **09**, 014 (2012)
[95] F. Abdulkhamidov, B. Narzilloev, I. Hussain, A. Abdujabbarov, and B. Ahmedov, Eur. Phys. J. C **84**, 420 (2024)
[96] A. Ashraf *et al*., Int. J. Geom. Methods Mod. Phys. 2650052 (2025)
[97] A. Bouzenada *et al*., Nucl. Phys. B **1021**, 117192 (2025)
[98] G. Török, Astron. Nachr. **326**, 856 (2005)
[99] J. Pétri, Astrophys. Space Sci. **318**, 181 (2008)
[100] A. Ditta *et al*., Phys. Dark Universe **47**, 101818 (2025)
[101] E. L. Junior, H. N. Lemos, and M. V. d. S. Silva, arXiv preprint arXiv: 2601.09482 (2026).
[102] M. Kolos, Z. Stuchlík, and A. Tursunov, Class. Quantum Grav. **32**, 165009 (2015)
[103] Z. Stuchlík and A. Kotrlová, Gen. Relativ. Gravit. **41**, 1305 (2009)
[104] Z. Stuchlík and J. Vrba, Eur. Phys. J. Plus **136**, 977 (2021)
[105] E. Sucu, S. Dengiz, and İ. Sakallı, (2025), arXiv: 2508.06725 [gr-qc].
[106] E. L. B. Junior, H. N. Lemos, and M. V. d. S. Silva, (2026), arXiv: 2601.09482 [gr-qc].
[107] O. Donmez, Astrophys. Space Sci. **293**, 323 (2004), arXiv: gr-qc/0406073
[108] O. Donmez, Appl. Math. Comput. **181**, 256 (2006), arXiv: gr-qc/0512104
[109] O. Donmez, O. Zanotti, and L. Rezzolla, Mon. Not. Roy. Astron. Soc. **412**, 1659 (2011), arXiv: 1010.1739[astro-ph.HE]
[110] O. Donmez, Eur. Phys. J. C **85**, 1019 (2025)
[111] K. Akiyama *et al*. (Event Horizon Telescope), Astrophys. J. Lett. **930**, L17 (2022), arXiv: 2311.09484[astro-ph.HE]
[112] A. G. Abac *et al.* (LIGO Scientific, VIRGO, KAGRA), (2026), arXiv: 2603.19019 [gr-qc].